1-1-2012

Optical Coherence Elastography Techniques for Carotid Arterial Wall Imaging

Felix Nolte
Ryerson University

OPTICAL COHERENCE ELASTOGRAPHY TECHNIQUES FOR CAROTID ARTERIAL WALL IMAGING

by
Felix Nolte
Bachelor of Engineering, 2010
Baden-Wuerttemberg Cooperative State University, Karlsruhe

A project
presented to Ryerson University
and Karlsruhe University of Applied Sciences

in partial fulfillment of the
requirements for the degree of
Master of Engineering
in the program of
Electrical Engineering

Toronto, Ontario, Canada, 2012

Author's Declaration

I hereby declare that I am the sole author of this thesis. This is a true copy of the thesis, including any required final revisions, as accepted by my examiners.

I authorize Ryerson University to lend this thesis to other institutions or individuals for the purpose of scholarly research.

I further authorize Ryerson University to reproduce this thesis by photocopying or by other means, in total or in part, at the request of other institutions or individuals for the purpose of scholarly research.

I understand that my thesis may be made electronically available to the public.

Toronto, 17/09/2012

Felix Nolte

Abstract

In this thesis, elastography is evaluated in combination with optical coherence tomography (OCT). Two approaches to OCT based elastography, Digital image correlation (DIC) and Doppler optical coherence elastography (DOCE), are evaluated for an intravascular setup using *in vivo* images from a porcine carotid model.

DIC tracks the displacement of speckle patterns in consecutive frames, allowing the calculation of axial and lateral strain. Rapid speckle decorrelation was observed in preprocessed structural images, affecting the tracking and limiting the feasibility of this algorithm.

DOCE measures axial strain based on relative tissue velocities. Rotational movement of the imaging optical fibre was the biggest source of artefacts in this imaging mode, but could be removed with a newly developed algorithm, based on the phase change induced in a surrounding catheter. The standard deviation of phase after artefact removal, measured in a stationary phantom experiment, was ~0.2 rad, corresponding to a minimum detectable velocity of 792 µm/s at a Doppler angle of 20°. The sensitivity allowed the detection of arterial blood flow velocity and pattern and the detection of adjacent veins, but did not allow direct elastography.

Acknowledgements

When I think about science, I remember the dwarf that is standing on the shoulder of giants. This metaphor by Bernhard of Chartres always meant to me that our work is based on a giant body of previous achievements, going back to the development of logic in ancient Greece. The making of this thesis revealed another meaning to me. There are also human giants, who carry us in this world and contribute to science in manifold, immeasurable ways.

I want to thank my supervisor Victor Yang not only for his overwhelming knowledge, but also for his optimism, motivation and his support at any time of the day. It was a pleasure working with you and it revealed to me the joys of working in science.

I want to thank Dr. Höpfel for his patience in supervising a student many thousand kilometers away.

My parents, for encouraging and stimulating me in the continuous process of learning. In moments of doubt they were there for me, put me back on my feet, and helped me back onto my track.

Eve Kahama, for her emotional support and for standing by my side. Thanks for cheering me up and all the good times.

Carry Sun, for her feedback and the productive discussions. She gave me a new perspective when I needed it the most.

My coworkers, for inspiring pep-talk. It is amazing how much creativity can be unlocked after a 5 minutes coffee break.

My friends, old and new, for making me feel at home wherever I am in the world.

Table of Contents

List of Figures

List of Appendices

1. Introduction

Optical coherence tomography (OCT) is an imaging method to visualize the structure of soft tissue. Light is applied to tissue and a small portion is backscattered. An OCT system derives tissue structure from the interference characteristics of the backscattered light with a reference.

OCT can achieve an axial resolution of 1 µm [1], which is better than ultrasound imaging (US) with around 50 µm [2] and magnetic resonance tomography (MRI) with 120 µm [3]. The resolution of OCT allows a wide scope of applications, which is only limited by low penetration depth. OCT has been used to examine the retina, skin and muscle.

OCT based elastography, which is termed optical coherence elastography (OCE) observes tissue elasticity, when the tissue is imaged during application of stress. An OCE system consists of a loading system and an OCT imaging system. The tissue elasticity is incorporated in the elastic moduli, which state the stress-strain relationship.

Many techniques from US elastography can be transferred to OCE. The first approach was made by Schmitt [4] with cross-correlation. Duncan and Kirkpatrick [5], Ko et al. [6] and Rogowska et al. [7] followed and enhanced this approach. Kirkpatrick et al [8] later added the use of Doppler phase shifts in light from tissue movement to complement cross-correlation in case of large displacements. Cross-correlation techniques are based on static or quasi static load. The displacement and strain information is yielded from a single image or from the comparison of two images.

In contrast to static excitation, dynamic excitation gains information from a larger sequence of images. In a general form of these approaches, a constitutive equation for the tissue response is fitted to a known periodic excitation of the tissue. Liang et al. [9, 10] as well as Liang and Boppart [11] use a step function or a sinusoidal waveform for excitation and a Voigt body model for the tissue response. Adie et al. [12] apply Bessel functions in combination with audio frequency excitation.

An intravascular application of OCE could aid in the examination of atherosclerotic plaque by detecting thin fibrous caps. This feature indicates vulnerability of a plaque, because it is prone to rupture and to release a lipid clod into the blood circulation, causing a risk of a stroke or an intracranial infarct.

Intravascular elastography lacks a stationary *in vivo* setup. Rotating system components and respiratory movement cause a rapid decorrelation and complicate traditional approaches to elastography.

These challenges have been mastered with ultrasound, where the technique has been named intravascular ultrasound (IVUS). De Korte and van der Steen [13] proposed a line correlation approach that was validated by histology after *in vivo* imaging of a Yucatan mini-pig model of atherosclerotic plaque. Talhami et al. [14] use the Fourier transform scaling property and apply their approach *in vivo* without validation. Ryan and Foster [15] propose two-dimensional speckle tracking to determine displacement and derive strain from the displacement. This algorithm is tested with a vessel mimicking phantom. Shapo et al. [16] use a balloon catheter to apply higher stress and thus get a better signal to noise ratio. Speckle correlation is performed over several consecutive frames. This approach was tested in phantoms and *in vitro*, with atherosclerotic human femoral artery and rabbit aorta.

Intravascular OCE is a younger field of research. Chan et al. [17] enhance a speckle correlation approach with the application of knowledge over vessel properties. After applying speckle correlation, the displacement estimation is corrected with an energy function that considers data fidelity, strain field smoothness and arterial wall incompressibility. Van Soest et al. [18] overcome speckle decorrelation with a line correlation approach. In their approach, a-scans are acquired in phase with the excitation, creating two sets of a-scans: compressed and uncompressed. Adjacent a-scans belong to different sets, while suffering less from speckle decorrelation than consecutive b-scans. Although both approaches to intravascular OCE show promising

results in simulations or bench top experimental setups, no *in vivo* results have been reported yet.

In this thesis, two approaches to intravascular optical coherence elastography are presented: DIC and DOCE. The feasibility of these approaches is evaluated in experiments on a phantom and *in vivo* on porcine carotid arteries. All experiments are performed with a commercial OCT system, whose optical characteristics are examined as well, to examine accuracy amongst other things.

2. Basics

2.1. Definitions in Biomedical Imaging

Throughout this thesis some terms will be used that are common in biomedical imaging. In this chapter we will provide a definition of these terms to ensure proper use. The definitions made in this chapter agree with the definitions made in [19].

A-scan, a-line – A one-dimensional scan made along a radial line from the catheter up to a defined depth.

B-scan – A two-dimensional scan that can be constructed from all a-scans recorded during one revolution of the imaging optical fibre.

Polar coordinates – The original coordinate system of recorded scan data. Every pixel in this coordinate system denotes an angular position θ of the imaging optical fibre and a depth position z, describing the axial distance between the imaging optical fibre and the pixel. In a polar coordinate system, the imaging direction is usually either from left to right or from top to bottom.

Cartesian coordinates – A coordinate system that is used for the display of cross-sections of arteries. Every pixel is denoted by a x- and a y-coordinate. For display, an OCT image has to be transformed into this coordinate system. The imaging optical fibre is displayed in the middle of the image. An a-scan is shown as a radial line from the centre to the edges of the image.

2.2. Anatomy of the Carotid Artery

Basic knowledge about the anatomy and function of the carotid artery is necessary to interpret images that reveal structure and elasticity of the vessel wall. The carotid arteries provide the blood supply to the head and the brain. They are organized in three layers of tissue, which are arranged circularly around the lumen of the vessel (see Figure 1) and are composed of different materials.[20]

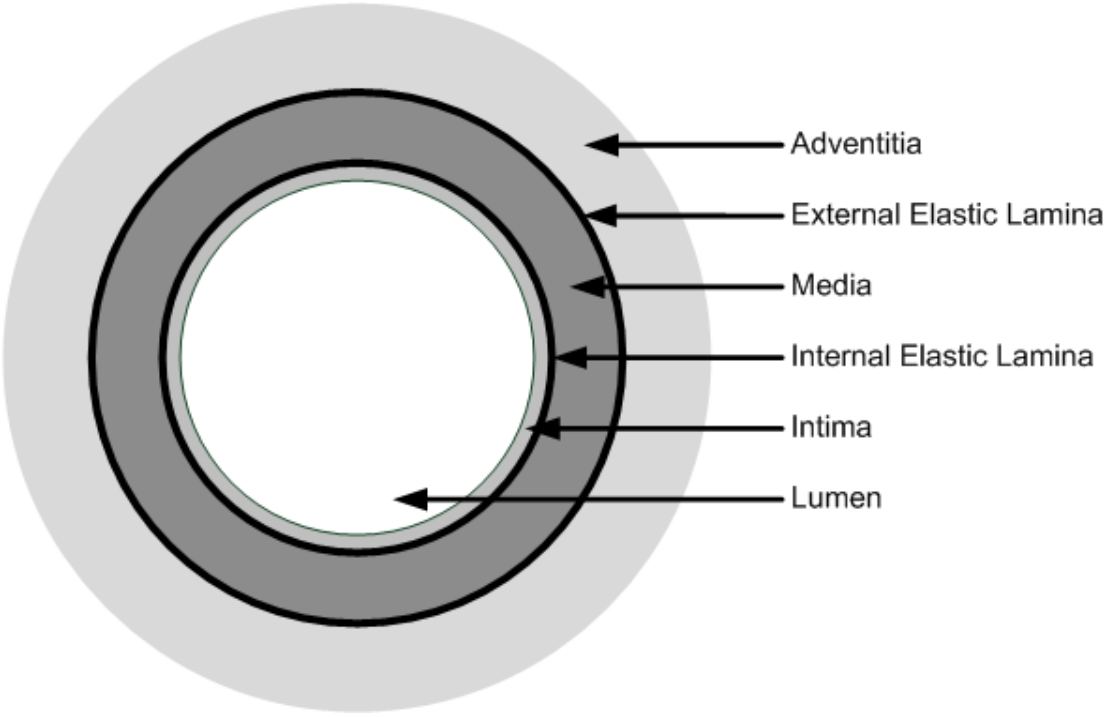

Figure 1: Anatomy of the Carotid Artery

The innermost layer is called intima. It is a thin layer that consists of endothelial cells, which form the barrier between the moving blood and the vessel wall. The intima has multiple functions, including the controlled exchange of nutrients and waste products between tissue and blood, and the prohibition of blood clotting.

Upon the intima follows the media, being separated by the internal elastic lamina. This layer has a varying consistency of elastic connective tissue and smooth muscle cells. Close to the heart, the connective tissue predominates, being capable of storing potential energy and thus supporting the pulsatile flow. The smooth muscle cells, which predominate further downstream in the carotid, are supposed to support the blood flow too and fulfill this task with active, autonomic contraction.

The adventitia is the outermost layer of the carotid artery. It is separated from the media with a membrane called external elastic lamina and it consists of loose connective tissue. The adventitia provides the connection to other surrounding tissues, embedding the blood vessel in the body.

An inflammation of the intima initiates the composition of atherosclerotic plaque. The inflammation causes a dysfunction of the material exchange functionality and allows macrophage white blood cells and low-density lipoproteins to intrude the intima. The biological reaction of the body can result in thickening of the vessel wall and building of atherosclerotic plaques.

Depending on the composition, these plaques are categorized into stable and unstable plaques. Stable plaques are mainly comprised of extracellular matrix and smooth muscle cells, while unstable plaques include more lipid deposits and foam cells. It is important to evaluate the composition of plaques, because unstable plaques have a risk to rupture and to release a lipid thrombus into the blood flow, which can cause a stroke or an intracranial infarct.

2.3. Stress-Strain Relationship

The different materials in atherosclerotic plaques can be characterized by different elastic properties. These properties can be changed due to pathological conditions and thus enable us to find features like soft fatigue tissue or calcifications.

The elastic properties are represented by a specific stress-strain relationship. This relationship can be strongly nonlinear and can only be defined in sections. In conditions (small deformation), when Hook's law holds, Young's modulus E describes the relationship. It is defined in (1 as the ratio of tensile stress σ and tensile strain ε.

$$E = \frac{\boldsymbol{\sigma}}{\boldsymbol{\varepsilon}} \tag{1}$$

Defining Young's modulus this way, raises the question how to define and how to calculate stress and strain in the blood vessel. The definition will follow in this chapter according to the definition in [21], before imaging methods and algorithms for the calculation of strain are introduced in the next chapter.

For the definition of a stress tensor, consider a small cube with edges parallel to the coordinate axes of a three-dimensional space. A force $\boldsymbol{T}$ acting on one of the surfaces of the cube can be modeled as a vector with three components, parallel to the three dimensions. The magnitude of the force varies with the size of the surface. Considering the surface to be infinitesimal small, results in a boundary vector of force per unit area. This vector is called stress vector $\boldsymbol{\sigma_i}$, consisting of the three components σ_{i1}, σ_{i2} and σ_{i3}.

In the example shown in Figure 2, the force acts on a surface perpendicular to the third dimension (striped surface). The stress components σ_{31} and σ_{32} act parallel to the surface and are called shear stress components. The component σ_{33} acts perpendicular to the surface and is named normal stress.

The complete description of stress on a cube consists of three stress tensors, acting on three perpendicular surfaces. This description is called stress tensor and includes three normal stress components σ_{11}, σ_{22} and σ_{33} as well as six shear stress components σ_{12}, σ_{13}, σ_{21}, σ_{23}, σ_{31} and σ_{32}.

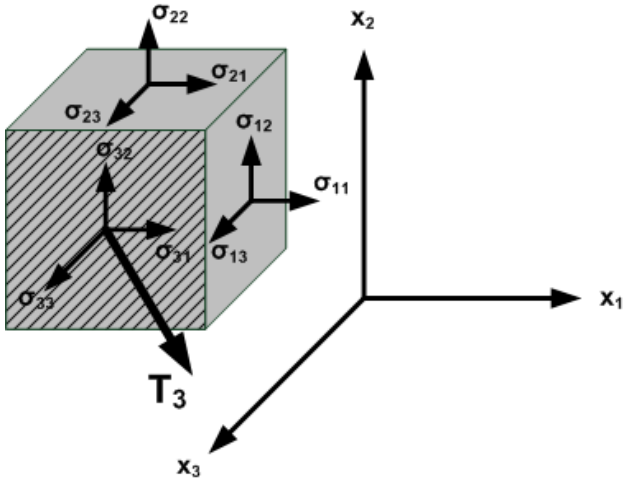

Figure 2: Definition of stress tensor

Strain can be explained best with an example: Consider a rubber band with the original length L_0. After stretching, the rubber band has a new length L. The strain ε is defined as the change of length per length element (see (2). Please note that this example explains strain in only one dimension.

$$\varepsilon = \frac{(L - L_0)}{L_0} \tag{2}$$

For a definition of a complete strain tensor in a three-dimensional space, a more complex definition is necessary. Consider a cube, being translated and deformed in this space, such that a point $P(a_i)$ is translated to a point $P(b_i)$, as it can be seen in Figure 3. The displacement of every point can be described with the vector $\boldsymbol{u}$, such that (3 holds. Please note that $\boldsymbol{u}$ is variable, so that adjacent points have an individual displacement.

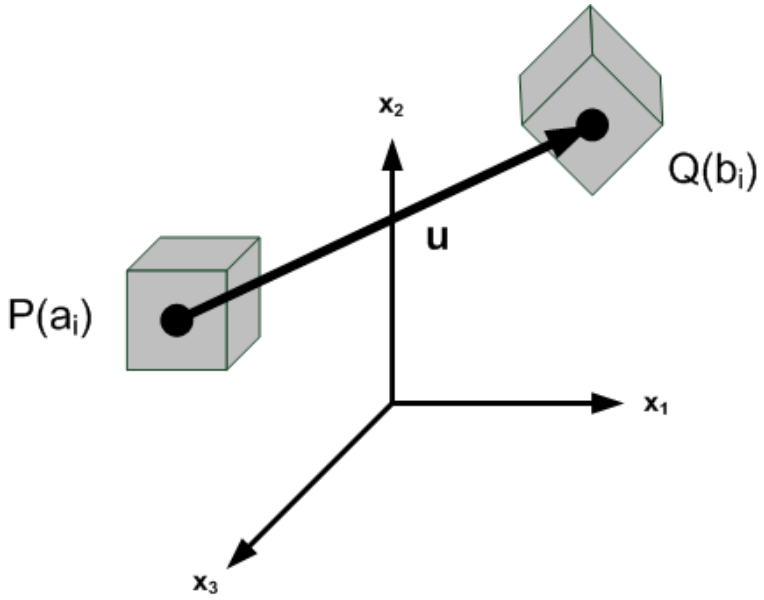

Figure 3: Definition of strain tensor

$$b_i = a_i + u_i \qquad i = 1,2,3 \tag{3}$$

Similar to the length in the rubber band example, strain is defined as the changing length between adjacent points in the cube. A complete strain tensor for a point consists of nine components: three normal strain components ε_{11}, ε_{22} and ε_{33} and six shear strain components ε_{12}, ε_{13}, ε_{21}, ε, ε_{31} and ε_{32}. The orientation of these components is analogous to the orientation of the components in a stress tensor.

Based on different imaging methodologies, stress-strain measurement and analysis can be performed in one or two dimensions in this thesis and the definition of a tensor can be simplified accordingly.

2.4. Optical Coherence Tomography

2.4.1. Time Domain Optical Coherence Tomography

The core of any OCT system is an interferometer. In the setup of Figure 4 this part is embodied by the Michelson interferometer. Light from a low coherence light source enters the interferometer and is split into two portions. One portion is send to the reference arm; the other portion interferes with the tissue in the sample arm. Light of the reference arm is reflected at a mirror. The position of this mirror can be varied, affecting the optical length of the reference arm. Light in the sample arm is focused onto the tissue sample. A small portion is backscattered and collected with the same optics system. Returning light from both arms creates an interference signal that is observed with a photo detector.

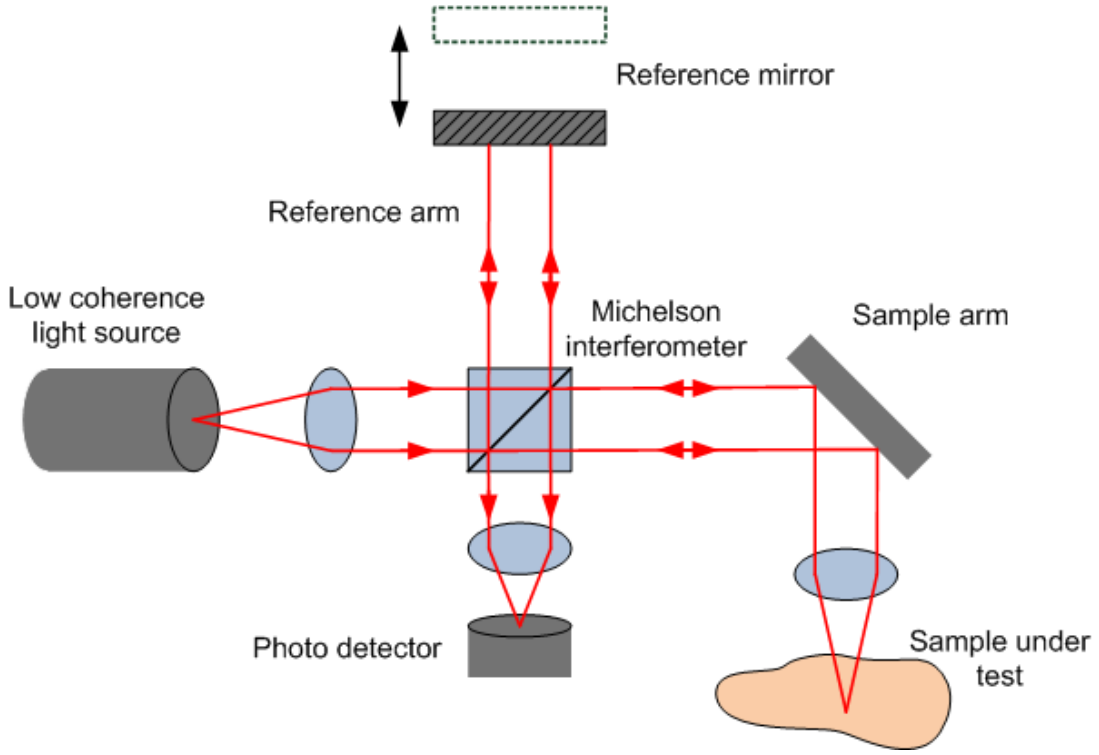

Figure 4: Time domain OCT system

The interference signal gives information about the reflectance at the imaging depth, which is determined by the runtime difference between the signals of both arms. By adjusting the length of the reference arm, the runtime difference can be altered.

The resolutions in axial and lateral direction of the beam are decoupled and can be optimized separately. The lateral resolution is determined by the focussing optics of the sample arm. The axial resolution is given in (4, where Δz is the axial resolution, λ is the group wavelength of the source and $\Delta\lambda$ is the bandwidth of the source.

$$\Delta z = \left(\frac{2ln2}{\pi}\right)\frac{\lambda^2}{\Delta\lambda} \tag{4}$$

The axial resolution in TDOCT systems is dependent on parameters of the light source. The group velocity is dictated by absorption characteristics of tissue so that research in this area is focussed on broadening of the bandwidth.

TDOCT was the form of OCT that was discovered first. It is reported to have axial resolutions down to 1 µm, which is superior to other imaging modalities. The imaging speed however is determined by the sweep speed of the reference mirror and further research was directed to overcome this mechanical constraint.

2.4.2. Frequency Domain Optical Coherence Tomography

Frequency domain optical coherence tomography (FDOCT) achieves faster scanning than TDOCT using signal acquisition in frequency domain and subsequent Fourier transformation. The mirror in the reference arm is stationary, which allows for high a-scan acquisition frequencies. There are two types of FDOCT systems: spectrometer based and swept-source. The latter one is also referred to as optical frequency domain imaging (OFDI).

In spectrometer based FDOCT, the interference signal is split spatially with a Bragg grating or a prism. The frequency-resolved signal is then acquired with an array of charge-coupled devices. Despite these changes, the optical setup of a FDOCT system is similar to a TDOCT system.

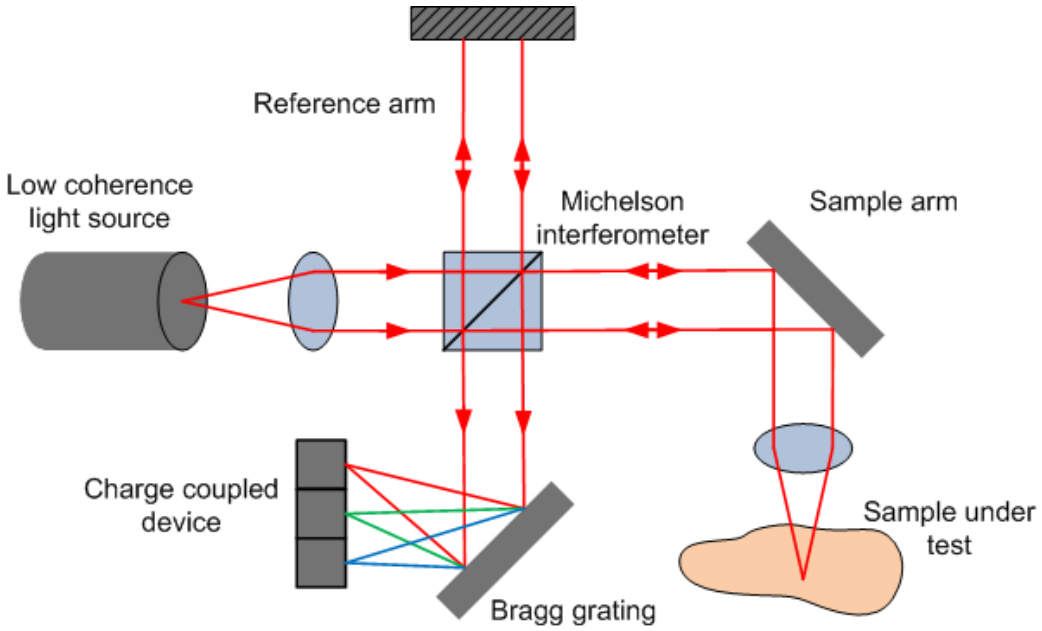

Figure 5: Frequency domain OCT system

In Optical Frequency Domain Imaging (OFDI) [22] the optical system can be further simplified. As opposed to spectrometer based FDOCT the frequencies are separated temporally instead of spatially. The laser has a small spectrum, but sweeps over a wide frequency range. The remaining optical setup is comparable to TDOCT, except for the reference mirror, which is stationary.

Using a small spectrum laser source allows to apply more power per wavelength, resulting in higher signal-to-noise ratios (SNR). In comparison to TDOCT advantages of 20 dB to 30 dB are possible [1].

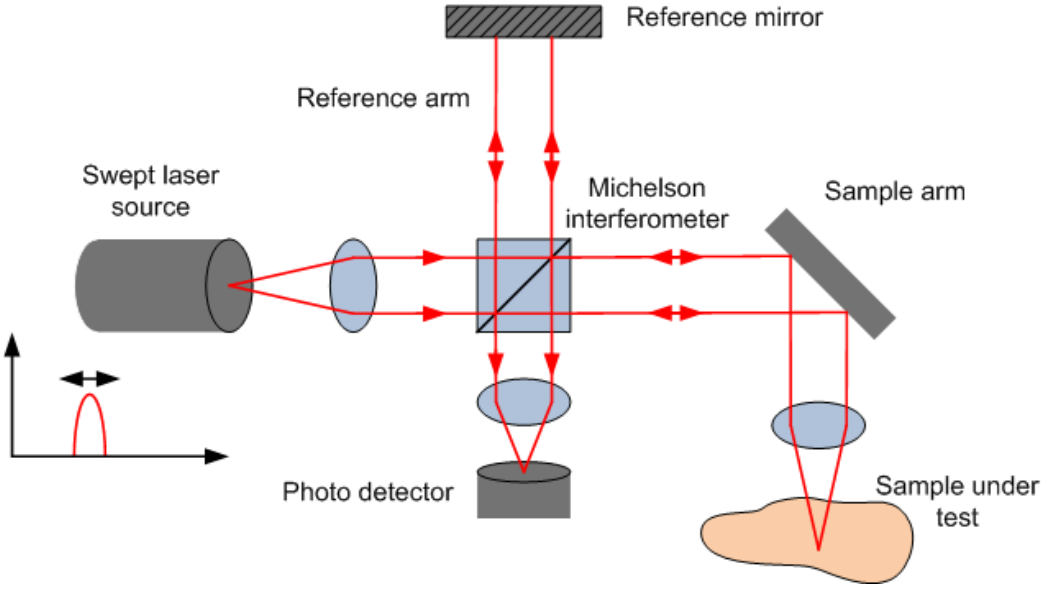

Figure 6: OCT system for OFDI

OFDI provides advantages that are ideal for intravascular OCE. High SNR is necessary to cope for power loss in the long sample arm. High scanning frequencies can be used to reduce effects of sample movement. The significance of these effects varies with the method of elastography that is used. It is thus important to find a method that makes best use of the advantages of OFDI.

2.5. Elastography

2.5.1. Cross Correlation Elastography

Cross-correlation based algorithms are the very basic elastography approaches, where speckle patterns are tracked in b-scans of the examined tissue. Static force is usually applied to deform the tissue. OCT b-scans are taken before and after the tissue deforms. Cross-correlation is then performed by taking a subset of pixels from the first b-scan and searching for the maximum correlation in the deformed b-scan according to (5. Both scans are taken in polar coordinates. The maximum of the correlation coefficient ρ gives an estimation for the displacement (u_x, u_z) of the subset.

$$\rho(u_x, u_z) = \frac{\sum_{x,z}[I_1(x,z) - \overline{I_1}][I_2(x',z') - \overline{I_2}]}{\sqrt{\sum_{x,z}[I_1(x,z) - \overline{I_1}]^2[I_2(x',z') - \overline{I_2}]^2}} \quad (5)$$

$I_1(x,z)$ and $I_2(x',z')$ are intensities at one pixel in the two scans, while $\overline{I_1}$ and $\overline{I_2}$ are the average pixel-values of the subsets. The pixels in the second subset are related to the pixels in the first subset, according to (6 and (7.

$$x' = x + u_x \quad (6)$$

$$z' = z + u_z \quad (7)$$

An adequate window size is essential for the performance of cross-correlation. If the window size is too small, the results might be inaccurate. Small features can get lost, if the window size is too big. The window size is application-specific, since the speckle pattern is dependent on properties of the light source and the examined tissue.

The strain fields are the numerical differentiation of the displacement vector, including two normal strain components and two shear strain components. Since the strain field calculation is a differentiation, it is susceptible to noise.

In addition to the measurement errors, [8] claims that cross-correlation is not feasible for very small or very large displacements. In case of small displacements (less than one pixel), no change might be measurable between consecutive b-scans. In case of large displacements, speckles might not be detected as correlating, resulting in faulty displacement estimation. The use of correlation techniques is thus limited to an adequate displacement. If this condition is not met, [8] proposes a maximum likelihood estimator for small displacements and the use of Doppler based optical coherence elastography for large displacements.

2.5.2. Doppler Optical Coherence Elastography

Doppler based OCE (DOCE) uses Doppler phase shifts in OCT signals to estimate tissue velocity. Integration of the movement over time leads to an estimation of displacement. DOCE was first described by Kirkpatrick et al in 2006 [8] and Wang et al [23] in the same year.

Both papers describe a calculation of displacement and strain in combination with a frequency-domain OCT system. This system obtains the combined spectral density of the reference arm and the light backscattered from the tissue under examination. The spectral density is given in (8.

$$I_d(f) = S(f)\left[1 + \int R(\tau)d\tau + 2R_{self} + 2\int \sqrt{R(\tau)}\cos(2\pi f\tau + \phi_0)\,d\tau\right] \qquad (8)$$

In this formula, $S(f)$ represents the spectral density of the light source, $R(\tau)$ is the normalized intensity, backscattered from the tissue at time τ, R_{self} is the interference of light backscattered from different scatterers in the tissue and ϕ_0 is the initial phase. The first three terms do not contribute to the OCT signal. Only the fourth term is relevant, so that the other three terms can be discarded and Fourier transform is performed on the fourth to get spatially resolved intensity, as it can be seen in (9.

$$I(z) = A(z)e^{-i\phi(z)} \qquad (9)$$

The phase term $\phi(z)$ is random along z, but constant over time, if the tissue is static. A displacement between successive a-scans induces phase change, as it can be seen in (10, where n is the refractive index of the tissue and k is the wavenumber of the light source.

$$\Delta\phi(z,t) = 2nk\Delta\mathrm{d(z)} \qquad (10)$$

From (10 the tissue velocity can be determined with Δt representing the acquisition time of one a-scan:

$$v(z,t) = \frac{\Delta d}{\Delta t} = \frac{\Delta\phi(z,t)\lambda}{4\pi n\Delta t} \qquad (11)$$

In an additional step, the axial strain rate can be obtained:

$$\dot{\varepsilon}(z,t) = \frac{\mathrm{v(z,t)}}{z_0} = \frac{\Delta\phi(z,t)\lambda}{4\pi n z_0\Delta t} \qquad (12)$$

The final step is the calculation of the displacement and strain, which is done by integration of the tissue velocity and strain rate over time.

$$d(z) = \int_0^T \Delta d(z,t)dt = \int_0^T \frac{\Delta\phi(z,t)\lambda}{4\pi n}\,dt \qquad (13)$$

$$\varepsilon(z) = \int_0^T \dot{\varepsilon}(z,t)dt = \int_0^T \frac{\Delta\phi(z,t)\lambda}{4\pi n z_0 \Delta t} dt \quad (14)$$

The displacement and strain that is obtained with this method is relative to unknown start conditions, so that no absolute strain can be declared. This step can be achieved with inverse problem approaches. Tissue Doppler approaches can only obtain deformation in axial scan-direction. However it is faster than cross-correlation based methods. In addition to this a velocity resolution of 2.6 nm/s is reported in [24].

2.6. Intravascular OCE

The intravascular application of OCE introduces new challenges during image acquisition. The spatial limitation constrains the size of imaging and loading system. Unstable imaging conditions and blood flow in the vessel lead to rapid speckle decorrelation.

Doppler based OCE has the potential to overcome the challenges, since it is independent from speckle patterns and provides instantaneous velocities without the influence of decorrelation of frames. It has to be noticed however that it has never been evaluated in an intravascular geometry.

Previous research has been performed on correlation-based approaches, providing results from simulations and from an *in vitro* experiment in a planar geometry. An overview over these approaches will be given in this chapter, to provide a comparison to the evaluation of new approaches in Chapter 3.

2.6.1. Variational Method

One of the few approaches to intravascular OCE was proposed in 2004 by Chan et al [17]. They address the vulnerability to noise and the speckle decorrelation and overcome these challenges by adding preliminary tissue knowledge to the estimation system.

Instead of traditional cross-correlation, a function for the variational energy of the tissue is established in (15. The velocity field is then adjusted so that the energy is minimized.

$$E[V(x,y)] = aE_D[V(x,y)] + bE_S[V(x,y)] + cE_I[V(x,y)] \quad (15)$$

The variational energy $E[V(x,y)]$ of the velocity field $V(x,y) = [u(x,y) \quad v(x,y)]$ is the weighted addition of the three terms data fidelity $E_D[V(x,y)]$, strain field smoothness $E_S[V(x,y)]$ and arterial wall incompressibility $E_I[V(x,y)]$. The weighting factors a, b and c are found experimentally.

In detail, the data fidelity term still uses cross-correlation, as it can be seen in its calculation in (16. The correlation coefficient $\rho_{x,y}$ is the same as in (5. Since the variational energy function has to be minimized, the correlation needs to be negated.

$$E_D[V(x,y)] = -\int\int \rho_{x,y}\big(V(x,y)\big)dxdy \quad (16)$$

The strain field smoothness and arterial wall incompressibility are constraints that introduce tissue knowledge. They are used to increase the energy cost of a velocity field that is unlikely due to known tissue behaviour. The calculation of these two terms can be seen in (17 and (18.

$$E_S[V(x,y)] = \int\int \|\nabla^2 V(x,y)\|^2 dxdy \quad (17)$$

$$E_I[V(x,y)] = \int\int \|\nabla \cdot V(x,y)\|^2 dxdy \quad (18)$$

According to [17], the minimization process is very sensitive to the initial velocity field. The authors address this problem with a multi-resolutional approach. A first guess of the velocity field is yielded with low resolution images and is used to initialize the estimation with full resolution. The minimization algorithm however is not mentioned in the paper.

In [25] the variational approach was tested on an *in vitro* porcine aorta specimen injected with lipid. The results show the potential to identify the fatty region. It has to be mentioned however that this experiment does not reflect the challenges from an intravascular setup and that involving previous knowledge might have its limitations in an inhomogeneous environment.

2.6.2. Optical Coherence Tomography Alternating-Line Elastography

Optical coherence tomography alternating-line elastography (OCTALE) was introduced in 2007 by van Soest et al [18]. This approach uses cross-correlation, but applies this method one-dimensional to adjacent a-scans instead of two-dimensional to complete b-scans. OCTALE avoids error from speckle decorrelation in consecutive b-scans at the cost of reducing displacement and strain estimation to the axial dimension.

The maximum of the correlation coefficient ρ_i in (19 thus only gives an estimation for the axial displacement δ. Averaging is performed over a window of m lines by n pixels. Axial normal strain is calculated by numerical derivation of the displacement.

$$\rho_i(\delta) = \frac{\sum[I_1(r_i) - \bar{I}_1(r_i)][I_2(r_i + \delta) - \bar{I_2}(r_i + \delta)]}{\sqrt{\sum[I_1(r_i) - \bar{I}_1(r_i)]^2 \sum[I_2(r_i + \delta) - \bar{I_2}(r_i + \delta)]^2}} \tag{19}$$

In order to produce displacement, an acoustic pressure is applied synchronously to the a-scan acquisition rate. This creates two sets of a-scans (I_1 and I_2), corresponding to a low and a high pressure scenario. Adjacent a-scans belong to different sets.

An acquisition and loading with exactly the same frequency puts high requirements to the synchronisation and the control system. This system however is the first approach that has been tested in a simulation of intravascular imaging and is less sensitive to nonuniform deformation than traditional cross-correlation.

3. Intravascular Porcine Carotid Optical Coherence Elastography

3.1. Image Acquisition System

The imaging system for this thesis (C7-XR, St. Jude Medical Inc. St. Paul, Minnesota, USA) uses a swept laser source to perform intravascular OCT. The sample signal is guided to the examination region with an optical fibre inside a catheter (C7 Dragonfly, St. Jude Medical Inc. St. Paul, Minnesota, USA) that is constantly flushed with saline. An optical system at the distal end of the fibre reflects the laser at 80° to the fibre axis and collects light backscattered from the vessel wall. The optical fibre rotates inside the catheter in order to acquire b-scans. The C7 Dragonfly catheter can be used in combination with a guide wire, providing increased manoeuvrability and stability during operation.

The C7-XR OCT system allows real time streaming of the raw scan data. This task is performed with a personal computer equipped with a data acquisition card (ATS9350, Alazartech). Next to the raw data, the computer also receives an a-scan trigger signal and a linear k-clock from the OCT system, as it is illustrated in Figure 7. Computations and display are performed on the GPU of the computer. The required software configuration is described in [26]. After digitization, the scan data is stored on a solid state disk and is available for offline signal processing.

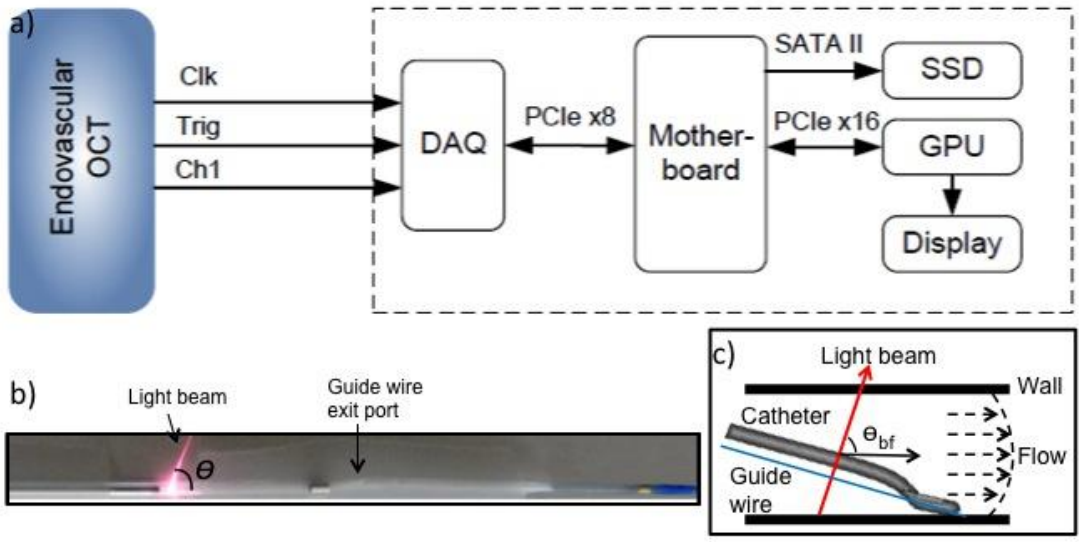

Figure 7: Image acquisition system

3.2. Determination of Beam Profile

Knowledge of the beam profile is important for the calculation of the phase. Overlapping areas in consecutive a-scans allow averaging to yield more precise phase values. In an experiment we determine the beam profile as a function of axial distance.

In order to measure the beam profile, the C7 Dragonfly imaging catheter is connected to a swept laser-source (Swept Laser SL 1325, Thorlabs) with a center wavelength of 1325 nm and a 3 dB tuning range of 125 nm. The spatial resolution of the beam profiler is given with 2.4 µm. The use of an alternative laser source is necessary to avoid the rotation of the C7-XR imaging system. A beam profiler is used to record the beam diameter and intensity distribution as a function of axial distance.

The beam profiler has a sensor array that is covered by a scanning slit. Due to rotation of the slit, these components are mounted in some distance, limiting the minimum distance of the imaging catheter to the sensor. The minimum distance can be measured with the C7-XR system. Corporate software allows the determination of distances, as it is shown in Figure 8 (a).

The beam profile is recorded after manual alignment, so that the beam is perpendicular to the sensor surface. A top view of a representative beam profile in Figure 8 (b) reveals significant side lobes in x- and y-direction.

Figure 8 (c) shows the beam diameter (average of x- and y-diameter after Gaussian fit, cut off at $1/e^2$) as a function of distance. The manufacturer specifies the focal spot size with 25 µm at a distance between 1.5 mm and 2.5 mm from the centre of the imaging optical fibre.

Based on these specifications, the Rayleigh range z_R can be calculated with 1.48 mm. It is known from Gaussian beam optics that the beam diverges in a straight line for $z \gg z_R$. This criterion allows us to apply linear fitting, as it is shown in Figure 8 (c). The beam waist should be located, where the linear approximation intersects the x-axis.

It can be seen from the approximation that the beam waist is estimated within the manufacturing tolerance. It has to be noticed however, that the measurement revealed considerable tolerance, because the available range of distances was limited. The measured should thus be judged as a trend and a confirmation of the specifications. For the calculation of pixel overlap (see section 3.4.3.1) we rely on the exact specifications of the manufacturer.

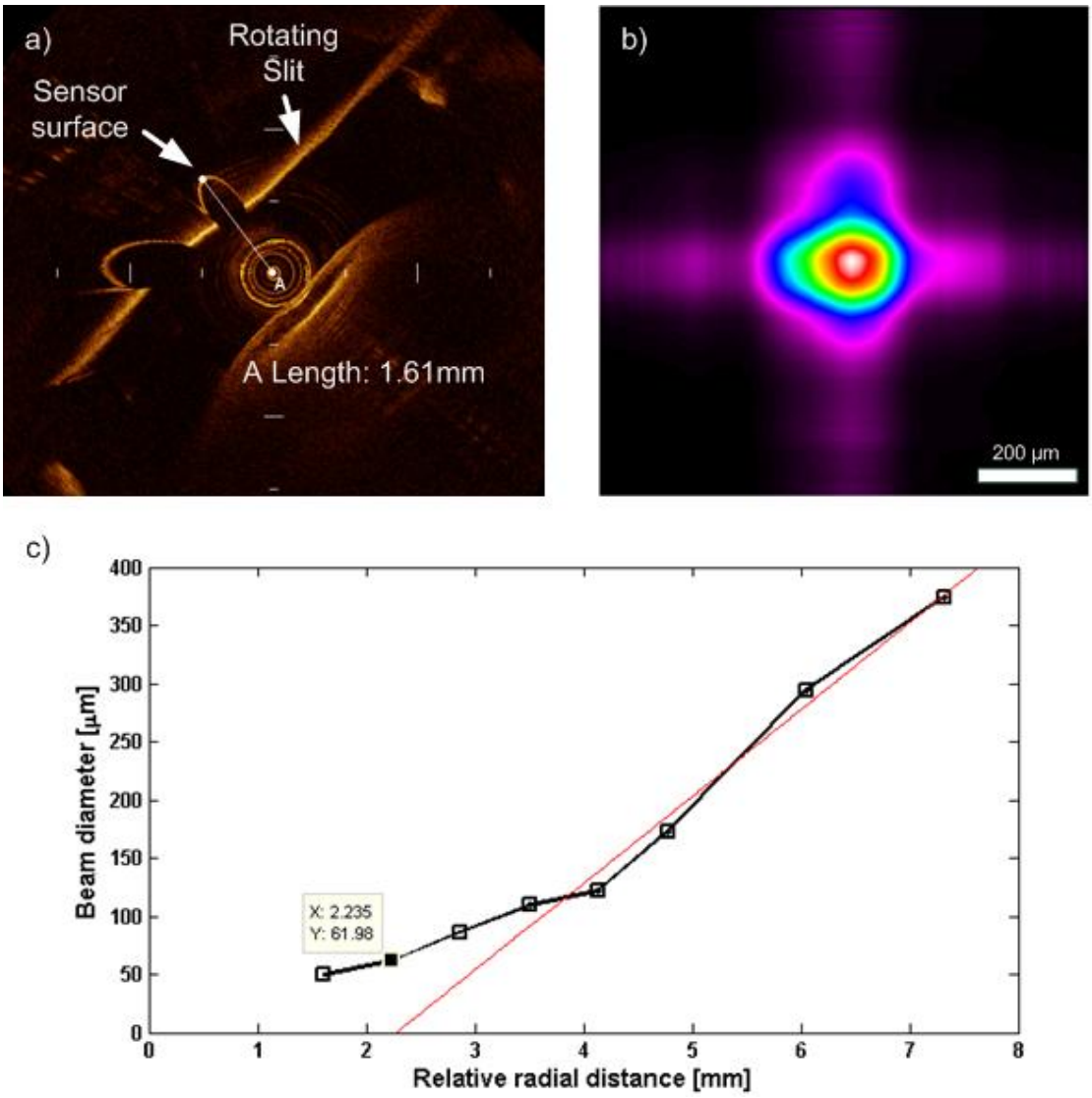

Figure 8: Results of beam profile measurement

a) Measurement of minimal distance between catheter and sensor in beam profiler

b) Representative beam profile, revealing side lobes

c) Beam diameter as a function of radial distance (black) and linear fitting for far field (red)

3.3. System Artefact Analysis

The image acquisition process includes various error sources. Some of these sources are systematic and can be reduced or completely removed. An analysis of the sources will be given in this section.

The missing stationarity of the catheter in the blood vessel and the imaging fibre in the catheter admits relative movement between components, inducing decorrelation in the structural image and phase offsets in the colour Doppler image.

A model of this movement helps to analyze the effects. The optical fibre is defined to be stationary in the centre of each b-scan in Cartesian coordinates. This perspective is legitimate, since every perceived movement is a relative movement between the fibre and other objects. Two objects with independent movement are typical components of an OCT image recorded with the C7 Dragonfly catheter: the catheter sheath and the tissue under examination. Both objects are able to perform a movement that can be modeled with three components:

1. Translation
2. Deformation
3. Rotation

A translation is a shift of the object in any direction. A shift of the tissue can be caused by respiratory movement of the patient. The catheter can be shifted due to blood flow or excitation from the optical fibre. A translation causes decorrelation of the structural image and induces Doppler phase shift for complete a-scans, when the movement vector includes an axial component.

A deformation happens, if an object changes its shape. The effects are similar to a translation. Decorrelation can be seen in the structural image and Doppler phase shifts in the colour Doppler image. As opposed to a translation, these phase changes can vary within the object and thus within one a-scan.

Translations and deformations can continue over several, consecutively acquired a-scans. An object, being in motion during this time, e.g. a square moving towards the observer (Figure 9 (a)), would be perceived deformed. The square would thus appear as a diamond (Figure 9 (b)).

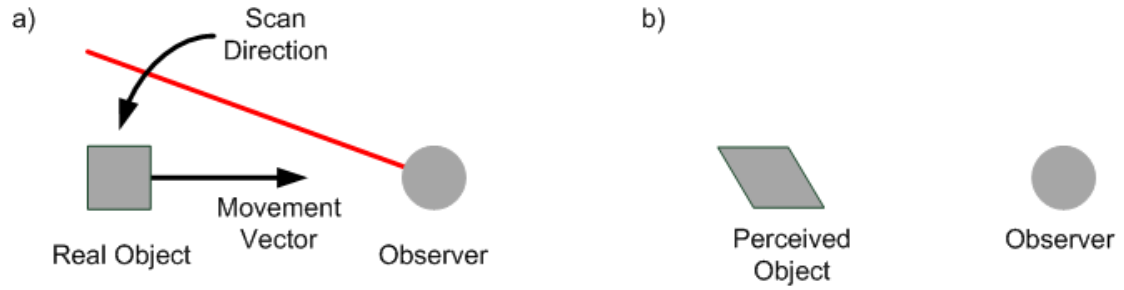

Figure 9: Effects of transition and deformation

A rotation of an object with the optical fibre as axis of rotation is hard to be perceived in Cartesian coordinates. It can be seen best in polar coordinates, where it causes a shift of the structural image as well as the phase image in lateral direction. In the structural image this shift is accompanied with decorrelation. The phase image undergoes no further change, as long as the optical fibre is aligned with the centre of rotation.

A model with a stationary optical fibre allows a good explanation of object movement, but it is hard to account for movement of the optical fibre itself. Effects resulting from movement of the optical fibre are visible indirectly as translations.

Despite physical artefacts in the sample arm, the OCT system is a source of system errors. Vakoc *et al* [27] report timing induced phase jumps in OFDI systems, causing offsets between adjacent a-scans. Furthermore the signal processing in the OCT system can induce a slow rotation of the complete image, causing an additional shift of structural and phase image. A linear sweep over a frequency range in combination with Fourier transformation results in windowing effects.

3.4. Experiments

The intravascular imaging system was used to acquire images in a porcine carotid model *in vivo*. The images were used to evaluate two new approaches to intravascular OCE: DIC and DOCE. The image acquisition procedures and the approaches, including the results, can be found in this section.

3.4.1. *In vivo* Image Acquisition Procedure

In vivo imaging experiments have been performed on Yorkshire pigs with healthy carotid arteries. The animals for this experiment were ~6 month old, weighting between 50 kg and 70 kg. Previous to the procedure, they were housed for one week in a vivarium at St. Michael's hospital in Toronto.

Upon sedation with ketamine, the pigs were anesthetized with continuous inhalation of isoflurane. Vital functions were observed with a physiologic monitor. The procedure was started with an incision in the groin. An 8-French catheter was inserted into the femoral artery and constantly flushed with heparinised saline. Through this catheter, the carotid artery is selected with a 5-French catheter and a guide wire. The positioning process is aided with x-ray imaging. Once the carotid is located, the 5-French catheter is replaced with a 6-French shuttle catheter that can be used to install a vessel protecting device (AngioGuard, Cordis). A rotating haemostatic valve with two three-way cocks is attached to the proximal end of the shuttle catheter. The three way cocks can be used to inject saline with a contrast agent (Omnipag) or heparinised saline.

At this point the procedure diverges. In the first animal, the imaging catheter was inserted, using the wire of the AngioGuard as a guide wire. In the second animal, an additional balloon catheter was used to fix the imaging catheter to the vessel wall.

With the imaging catheter in place, continuous image acquisition was activated on the C7-XR system. In order to remove blood within the lumen, saline with contrast agent was injected with an automated pump at ~5 cc/sec. Sequences of OCT data was recorded with a personal computer configured as described with the image acquisition system.

In an alternative process, a mixture of blood (1.5% percent of volume) and saline was injected instead of saline with contrast agent. This variation was used to test the feasibility of intravascular OCT for blood flow imaging.

3.4.2. Digital Image Correlation

The newly generated dataset of OCT images is used to evaluate different approaches to OCE. Motivated by previous research on correlation-based algorithms, we evaluated the feasibility of DIC in an intravascular setup. In order to reduce influence of noise, calculations are performed with preprocessed structural images in Cartesian coordinates generated with corporate software (Operating System of C7-XR, St. Jude Medical Inc. St. Paul, Minnesota, USA).

The use of preprocessed images may have a negative influence on the estimation of displacement and strain, but it is useful for the evaluation of preliminary process steps, like the correction of bulk movement. The results however have to be considered as preliminary results.

Due to the conditions during image acquisition, bulk movement can appear, when the imaging catheter moves or rotates relative to the surrounding tissue. All bulk movement except for rotation can be reduced by aligning the lumen center in sequential images to the image center. This process is illustrated in Figure 10. The lumen outline is detected with intensity thresholding. Subsequent Hough transformation finds the centre of the lumen. Irregular outline and nonuniform deformation limit the precision of this algorithm.

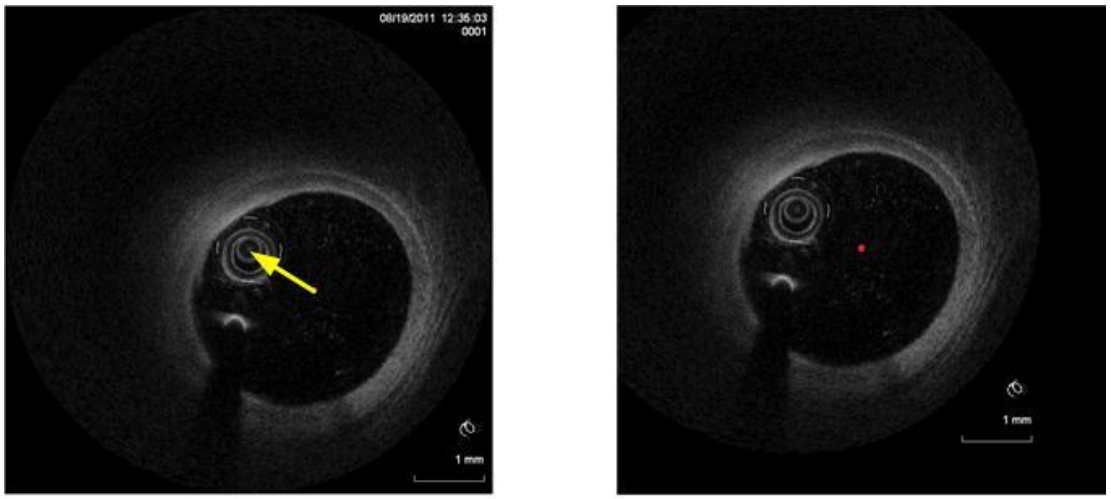

Figure 10: Centering of the lumen in the structural image

a) Structural OCT image before centering (with estimated centering vector),

b) Same image after centering (red dot indicates the center of the lumen)

After removal of bulk motion, the images are transformed into polar coordinates using bilinear interpolation. The transformation is necessary for the subsequent estimation of displacement and strain.

The estimation is based on cross-correlation, but introduces the gradients of the displacement $\frac{\partial u_x}{\partial x}, \frac{\partial u_x}{\partial z}, \frac{\partial u_z}{\partial x}, \frac{\partial u_z}{\partial z}$ as additional estimation parameters. A similar method was performed in [28] for the estimation of surface deformation. The maximum of the new cross-correlation coefficient from 20 gives an estimation for displacement and for the gradients of the displacement vector. The estimation results are computed iteratively with the Newton-Raphson method [29].

$$\rho\left(u_x, u_z, \frac{\partial u_x}{\partial x}, \frac{\partial u_x}{\partial z}, \frac{\partial u_z}{\partial x}, \frac{\partial u_z}{\partial z}\right) = \frac{\sum_{x,z}[I_1(x,z) - \bar{I}_1][I_2(x',z') - \bar{I}_2]}{\sqrt{\sum_{x,z}[I_1(x,z) - \bar{I}_1]^2[I_2(x',z') - \bar{I}_2]^2}} \qquad (20)$$

The underlying motion model is described in 21 and 22. The estimated gradients of the displacement are identical with the normal and shear strain values, so that they no longer need to be calculated by numerical derivation.

$$x' = x + u_x + \frac{\partial u_x}{\partial x}\Delta x + \frac{\partial u_x}{\partial z}\Delta z \tag{21}$$

$$z' = z + u_z + \frac{\partial u_z}{\partial x}\Delta x + \frac{\partial u_z}{\partial z}\Delta z \tag{22}$$

In order to reduce the computational cost, the estimation is constrained to a user-defined region of interest. For additional reduction, the estimation was not performed at every pixel, but with a user-defined density of data points. The complete displacement and strain fields were then interpolated linearly from the three closest data points. The resulting displacement fields and strain fields are finally transformed into Cartesian coordinates, using bilinear interpolation, as described in [30].

The results presented in this thesis are calculated for two sequential frames that are shown in Figure 11. Components of the vessel wall have been labeled in (a) according to [31]. Components of the imaging system have been labeled in (b). In order to get a reference for the estimated displacement and strain, the change of the vessel wall is observed in the structural image. After centering of the lumen almost no bulk movement or rotation was perceptible. Artefacts from incomplete flushing appear between 6 o'clock and 10 o'clock, while clear results are received between 10 o'clock and 12 o'clock. In the latter section, the diameter of the media changes, so that axial normal strain should be observed.

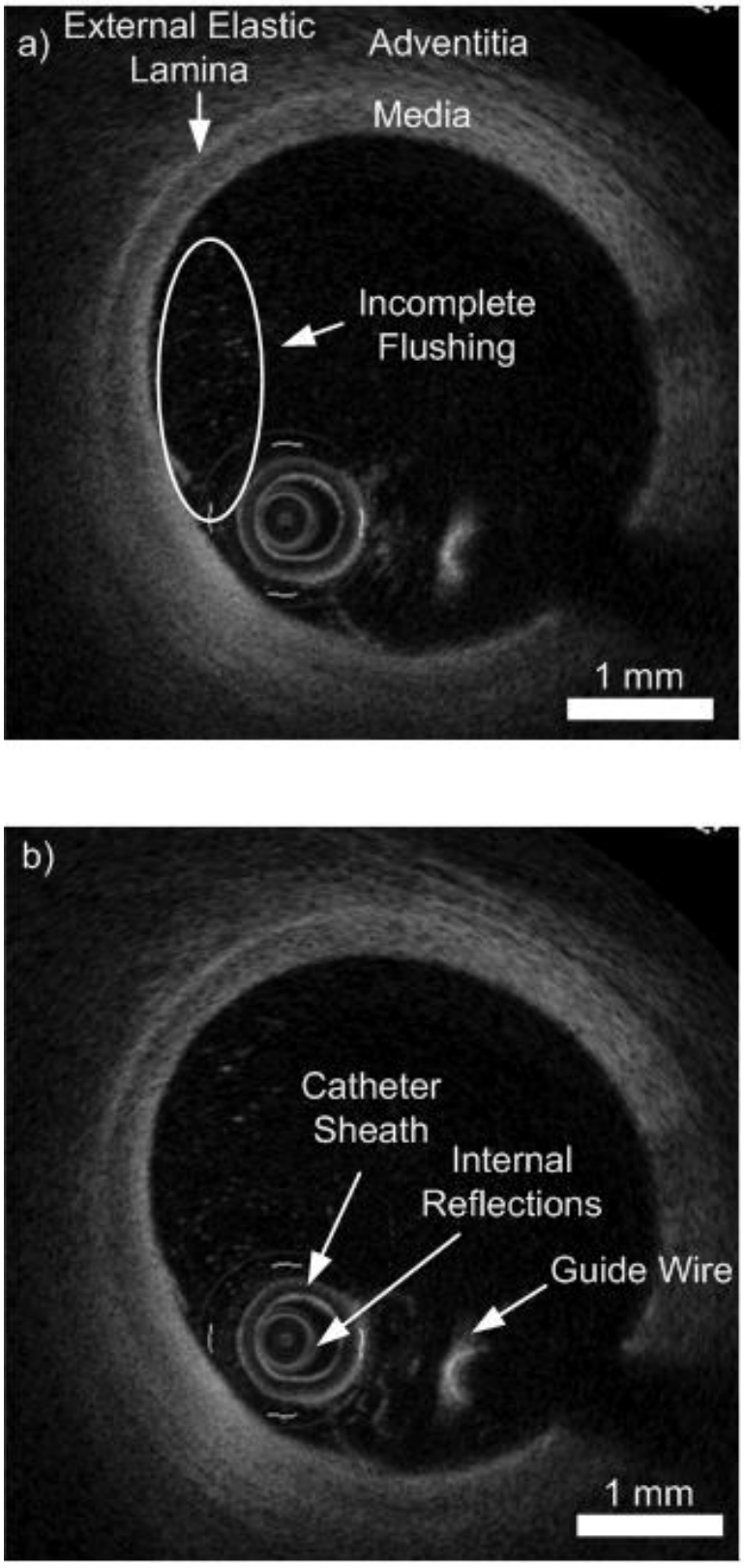

Figure 11: Structural OCT image of porcine carotid artery

The vessel wall on the left side of the image has been chosen as a region of interest (ROI) and displacement and strain estimation has been performed with a correlation window size of 51 x 51 pixels at every fifth pixel. The maximum displacement was constrained to 13 pixels.

Figure 12 shows the estimated displacement in axial and lateral direction, relative to the center of the lumen. The displacements in the ROI are measured in pixels. Region A shows big lateral displacement, which however is not observed from the structural image. We assume that this is measurement artefact induced by incomplete blood flush. Despite this artefact, only small movement can be observed in axial and lateral direction.

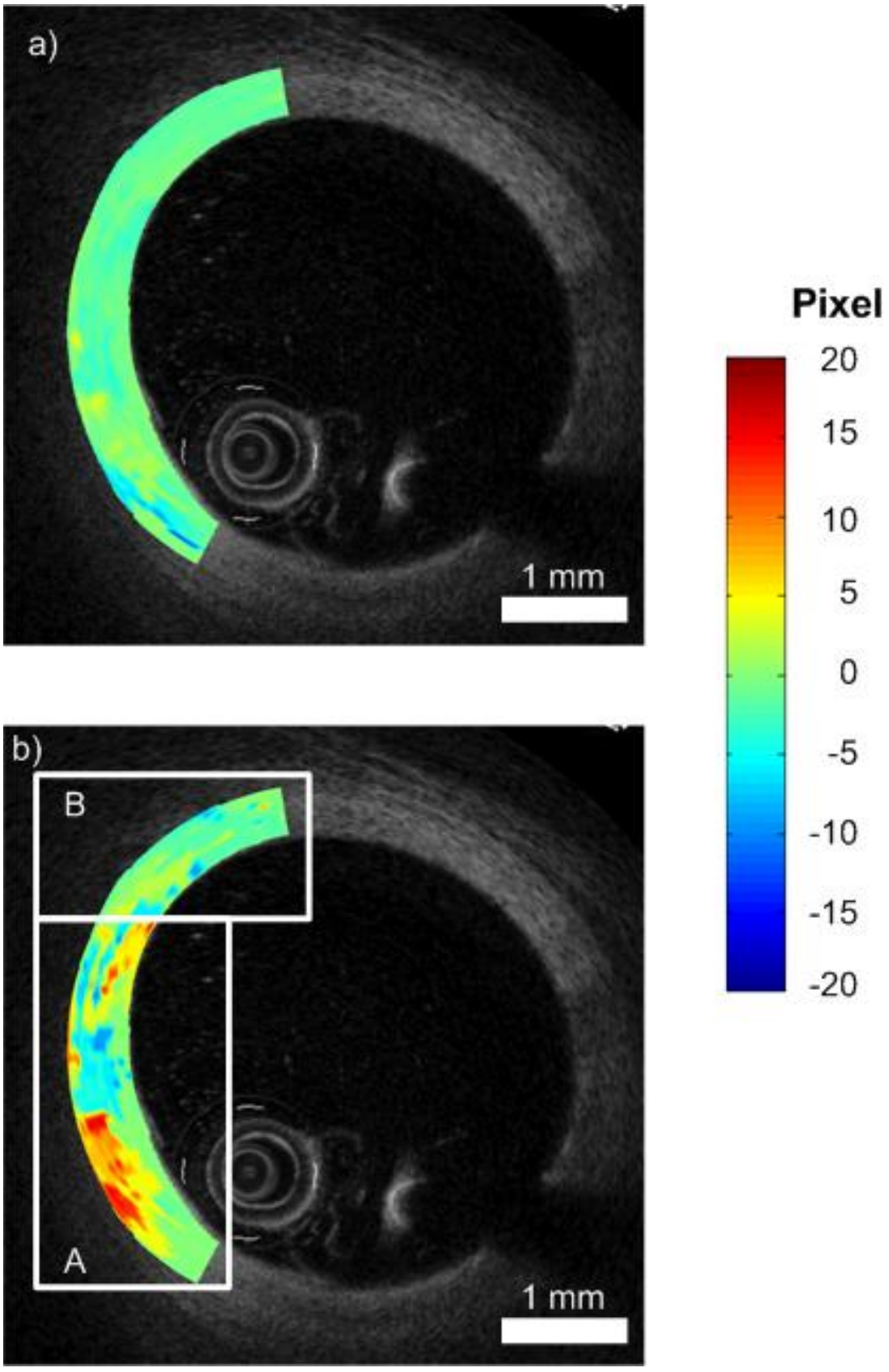

Figure 12: a) Axial displacement, b) Lateral displacement

Strains are obtained simultaneously with displacements in the ROI. Normal strain and shear strain elastograms are shown in Figure 13. The strain values are measured in percent. All displacement and strain fields are calculated in polar coordinates.

The unflawed region between 10 o'clock and 12 o'clock allows a clear distinction between the media and adventitia in the axial normal strain image (Figure 13 (a)). Lateral normal strain (Figure 13 (b)) and axial shear strain (Figure 13 (c)) show no visible changes. The lateral shear strain (Figure 13 (d)) reveals a strain pattern that resembles the external elastic lamina, but it is accompanied with an irregular strain distribution in media and adventitia.

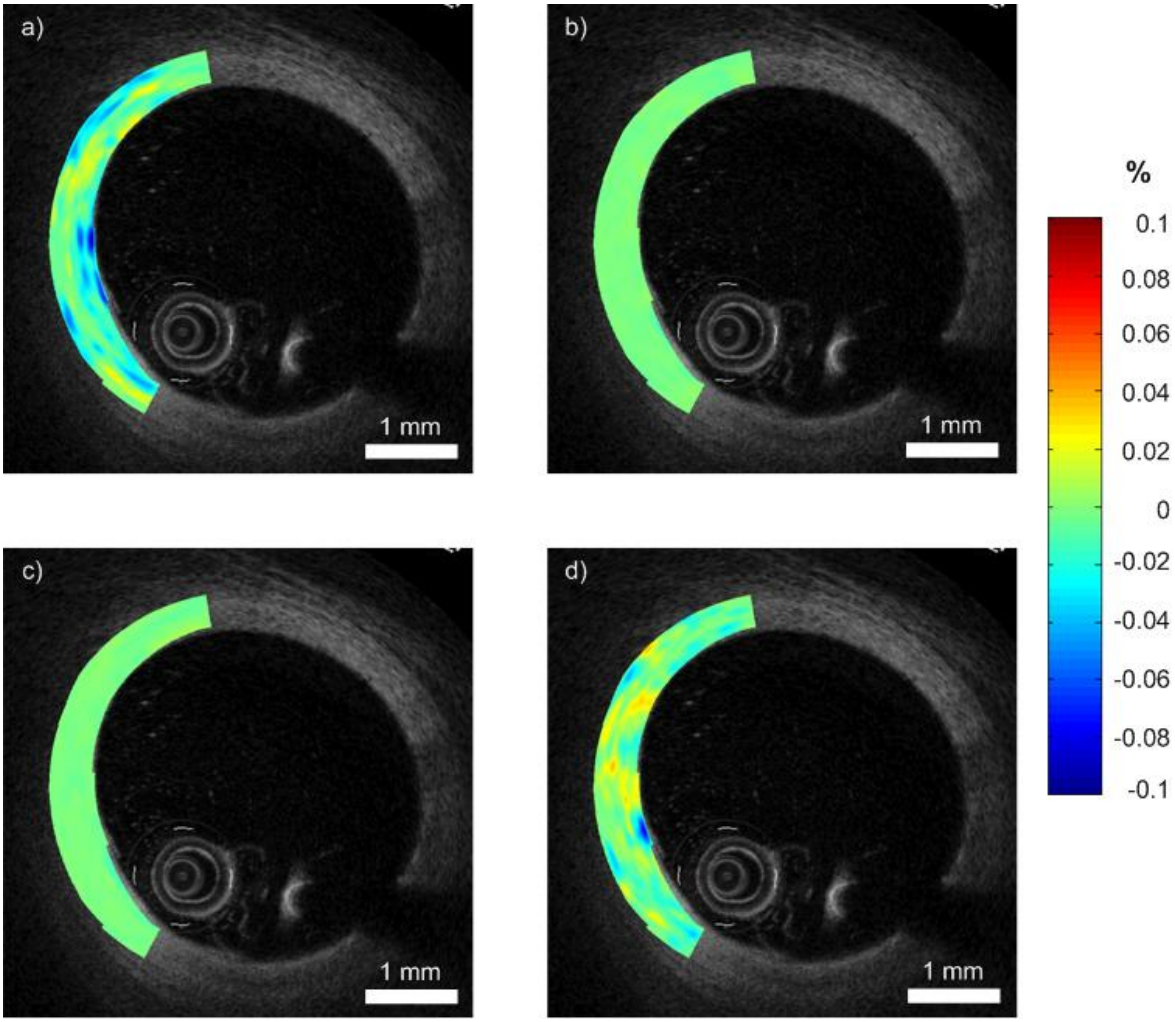

Figure 13: a) Axial normal strain, b) Lateral normal strain,

c) Axial shear strain, d) Lateral shear strain

3.4.3. Doppler-Based OCE

Previous research on coherence-based intravascular OCE reported rapid speckle decorrelation and presented different approaches to address this challenge. Our findings from the previous section confirm the difficulties of coherence-based approaches and motivated the evaluation of alternative approaches.

As mentioned in section 3.1, the image acquisition provides digitized and unformatted scan data in the frequency domain. This data allows the calculation of Doppler phase shifts, which can be displayed in colour Doppler maps. Based on Doppler phase shifts, axial strain can be calculated as described in section 2.5.2. The complete algorithm is depicted in Figure 14. All calculations in this algorithm are performed in Matlab. A description of the scripts can be found in Appendix 1.

Windowing effects in relation with Fourier transformation are addressed with a Blackman-Harris window to minimize side lobes. Fourier transformation of windowed a-scans produces a complex signal.

The structural image is given by the magnitude of the transformed a-scans. Each b-scan contains 2500 a-scans, providing a high scan-density. Colour Doppler images are generated with the Kasai autocorrelation technique [32]. Due to the high density, multiple a-scans overlap and can be used for averaging. We chose a window of 2 over 10 in axial and lateral direction, maintaining high resolution in axial direction and taking advantage of the lower lateral resolution.

The catheter is localized in the structural image with manual segmentation and the colour Doppler image is unwrapped for this region using quality guided unwrapping [33]. The median phase is determined for each a-scan and subtracted from each pixel beyond the inner catheter wall.

Rotation of the b-scan can be removed with an alignment algorithm. The first frame in a sequence of structural images is taken as reference. A small window is drawn around a region with extraordinary structural features. The window is then correlated with the following frames and the maximum correlation gives an estimation of the shift that is corrected by shifting the image in the opposite direction. In sequences with strong deformation, the windowed region might be deformed, affecting the performance of the alignment. We addressed this behaviour by periodically replacing the reference frame and the window with a newly aligned frame.

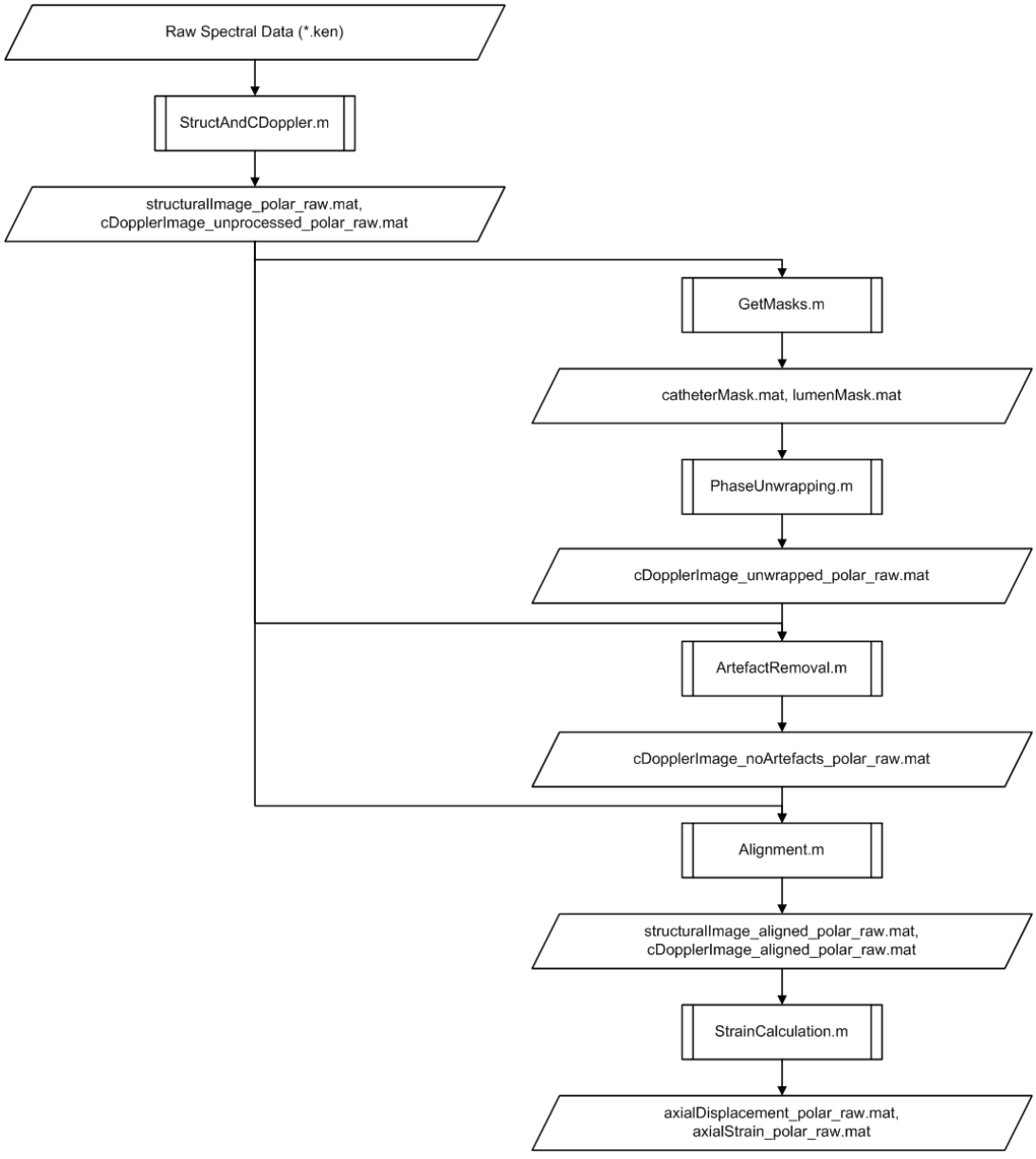

Figure 14: Flowchart of signal processing

3.4.3.1. Blood Flow Imaging

Blood vessels can be modelled as elastic tubes for the purpose of calculating stress and strain. A large quantity of factors influences stress and strain distribution in this model. Smooth muscle cells in the vessel wall cause active deformation. Blood pressure inside the vessel induces stretching. Blood flow has various effects on the wall, including shear stress, longitudinal stress and residual stress. Neighbouring organs like other blood vessels may be necessary to be considered in addition to these directly vessel-related factors. Knowledge about selected quantities can increase the precision of stress-strain models.

The average shear stress (SS) induced by blood flow is ~1 Pa [34]. Gijsen *et al.* [35] recognize that this quantity is several orders of magnitude smaller than the influence of blood pressure, but point out that small and/or oscillatory SS can cause endothelial dysfunction. In order to investigate this effect, they provide simulation-based quantitative results for SS in different regions of atherosclerotic plaque.

Fry [36] investigated, how flow, measured *in vivo* or *in vitro*, can be related to shear stress (see (23). According to his equation, the shear stress in flow direction σ_y can be calculated with the radius of the blood vessel R, the position on an axis in flow direction y, the pressure gradient along this axis $\partial p/\partial y$, the blood density ρ, the flow Q at the time t, the blood velocity ω along the axis y and the distance from the centre of the vessel r.

$$\sigma_y = \frac{R}{2}\frac{\partial p}{\partial y} + \frac{\rho}{2\pi R}\frac{dQ}{dt} + \frac{\rho}{R}\frac{\partial}{\partial y}\int_0^R \omega^2 r\, dr \qquad (23)$$

Simultaneous measurement of blood flow pattern and flow velocity has the potential to characterize the spatial and temporal variation of SS in the vessel wall. Additional measurement of the vessel wall provides a set of haemodynamic data including flow velocity and wall SS distribution *in vivo*. This set of data supports the study on fluid-wall interactions, leading to an understanding of the mechanical properties of the vessel wall.

Structural intravascular OCT imaging provides a measurement of the vessel wall thickness with unprecedented accuracy. This measurement can be coupled with blood flow measurement based on Doppler OCT (DOCT). To our knowledge this imaging mode has never before been evaluated. Our results on this field are presented in the manuscript in Appendix 2 and have been submitted to the Biomedical Optics Express.

Further research has the potential to provide additional data. Blood pressure can be calculated through a blood/wall coupling algorithm, combining blood flow and vessel mechanics in a model of the carotid artery. Elastograms of displacement and stress fields in the presence of pulsatile flow can be determined with a finite element model.

3.4.3.2. Doppler Optical Coherence Elastography of the Arterial Wall

Imaging of blood flow based on Doppler OCT revealed important data about the environment of the vessel wall. In addition to this data, Doppler based OCT has the potential to directly calculate axial strain in the vessel wall. We evaluated this application, using the signal processing algorithm as described above.

Structural images reveal anatomical features of the tissue in combination with the imaging system. Figure 15 shows two structural images, recorded with a free floating imaging catheter (a) and with the imaging catheter in combination with the balloon catheter (b).

In Figure 15 (a) biological features of the blood vessel have been labeled. The media can be identified as the thick layer limited by the external elastic lamina. Beyond the external elastic lamina the adventitia can be seen, characterized by an irregular speckle pattern. Between 4 o'clock and 6 o'clock dark areas can be seen between the external elastic lamina and the adventitia. Temporal changes of these areas indicate the presence of small blood vessels, known as vasa vasorum.

The imaging system itself can be seen in the centre of the structural image. Due to reflections inside the imaging system, concentric circles appear around the optical fibre. The catheter around the fibre is characterized by two circular reflections that can be unaligned with the catheter, but are concentric to each other. Since the catheter is nearly transparent, these reflections are less prominent than the internal reflections.

In combination with a balloon catheter, characteristics of the structural image can change. In the inflated state, the balloon fills the lumen, restricting blood flow. This behavior can be seen in Figure 15 (b). The inflated balloon also pushes the imaging catheter into the vessel wall, causing a nonuniform deformation of the vessel wall that is visible in the region between 4 o'clock and 6 o'clock.

Although the balloon is nearly transparent, it reveals noticeable attenuation, lowering the SNR in the wall beyond. Only the guide wire of the balloon can be seen clear in the balloon area, due to its bright reflection.

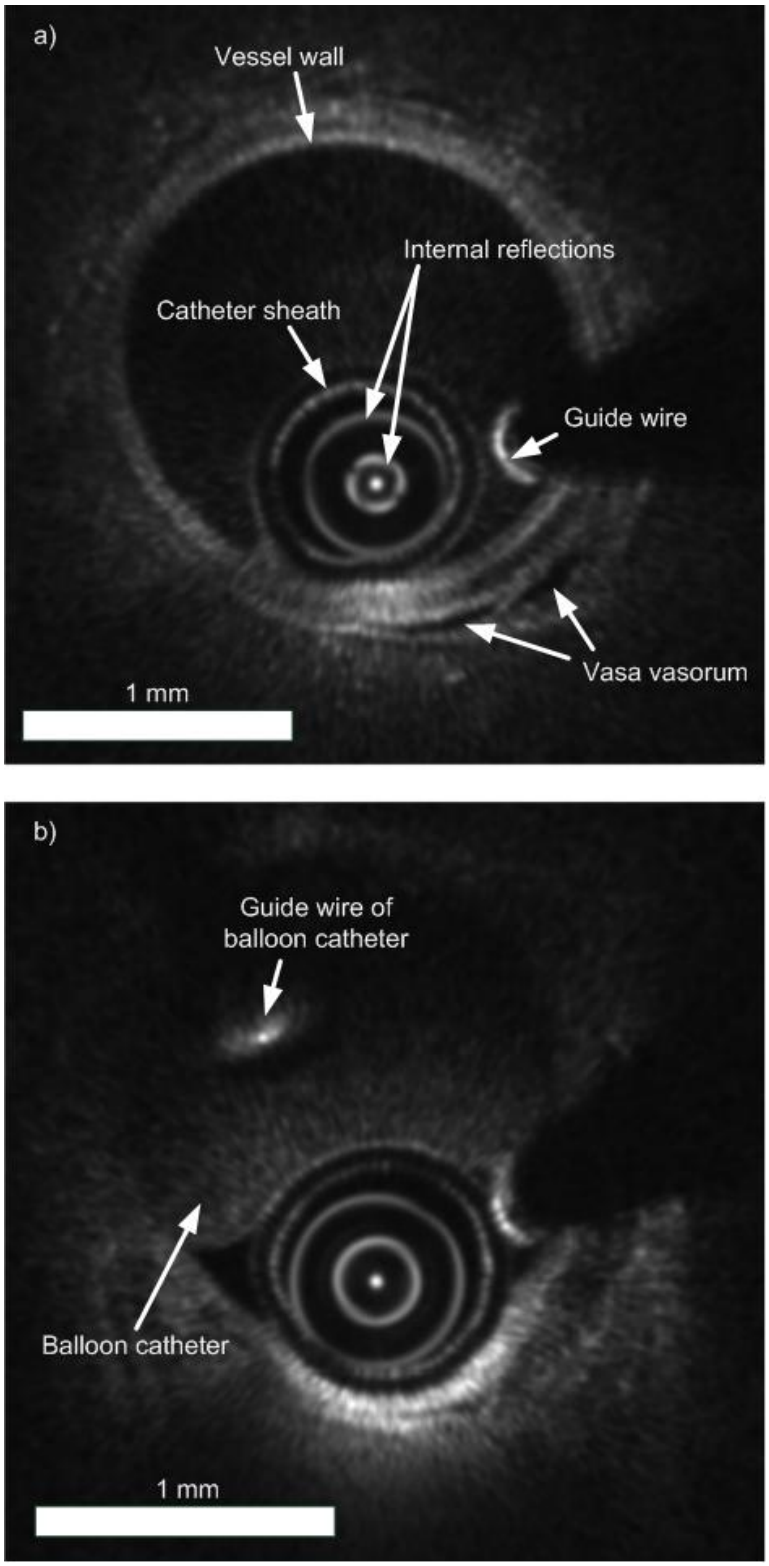

Figure 15: Features of typical structural images

Colour Doppler images were recorded with both imaging procedures. A comparison of these images without signal processing helps to identify prominent noise sources. The comparison in this thesis was based on the two colour Doppler images that are given in Figure 16. Please note that these images correspond to the structural images in Figure 15, but show a different section of the image, centering the catheter instead of the lumen.

The colour Doppler image recorded without a balloon catheter (Figure 16 (a)) belongs to the sequence presented in the paper. For the purpose of this thesis, a more detailed description supports the relation to the structural image.

Internal reflections appear as black circles in the centre of each image, lying over a noise floor with random phase values. The catheter is represented with two concentric circles, consisting of phase values that are constant along radial lines. These lines are continued in tissue, where they slowly disappear below the noise floor, as the SNR decays. In areas with an SNR close to 1, which is apparent in the far field and in the shadow behind the guide wire, random phase values appear.

Figure 16 (b) shows the colour Doppler image corresponding to the structural image with a balloon catheter in Figure 15 (b). It can be seen that the radial lines dominate the signal in the tissue in the same way like in the colour Doppler image without a balloon catheter. Moreover that, the same lines are now visible in the lumen too, replacing the flow profile. Between five and seven o’clock, an area of fast flow is visible.

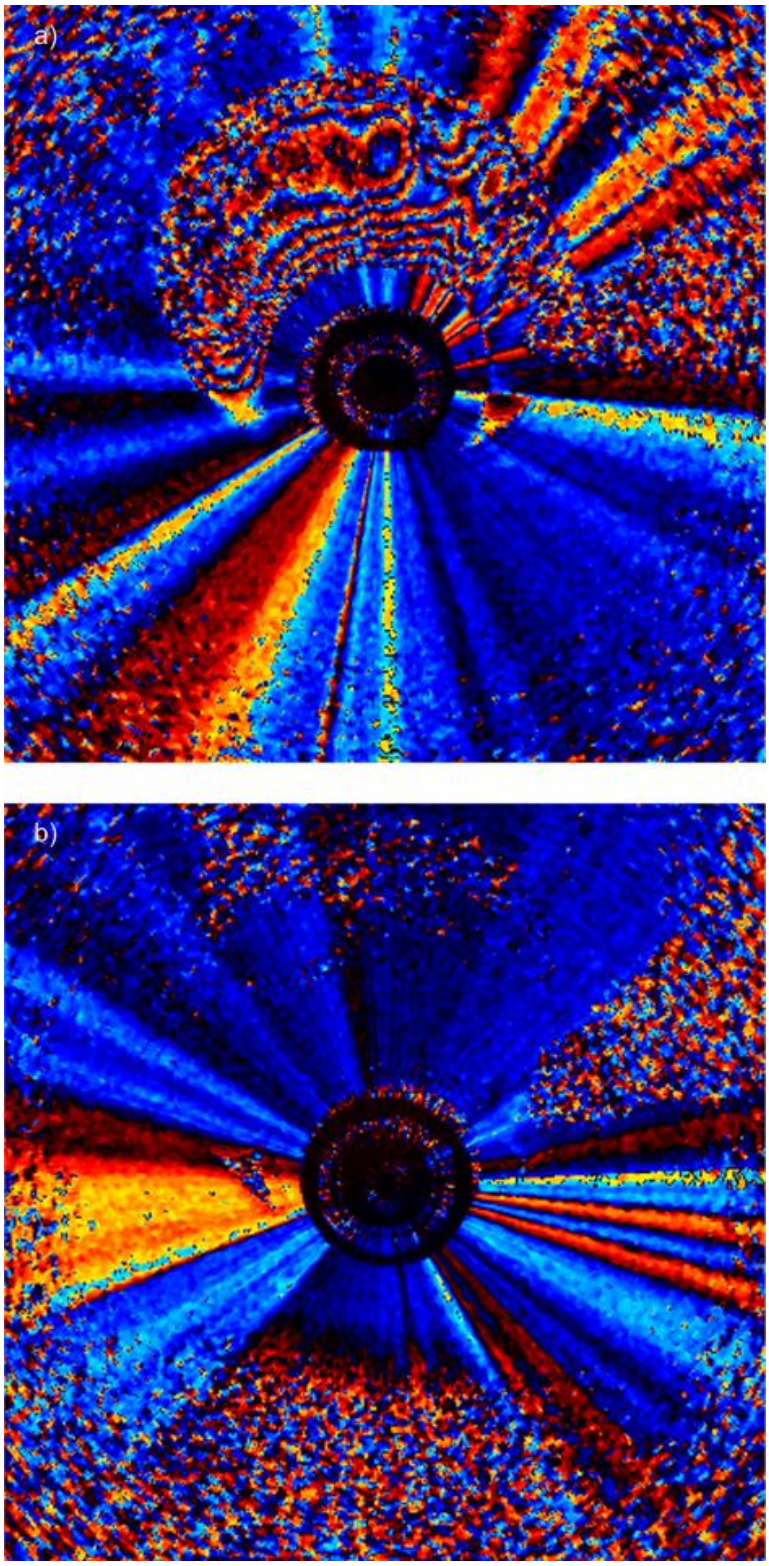

Figure 16: Artefacts in colour Doppler images

a) imaging without balloon catheterization, b) imaging with balloon catheterization

For the purpose of Doppler-based elastography, suppression of system artefacts in colour Doppler images is necessary to reveal tissue features. The result of this step can be seen in Figure 17. The images in part a and b of this figure correspond again to the colour Doppler images in Figure 16.

The temporal development of the artefact removal can be seen in the supplemental videos [Media1_Fig_5_e_f.avi, Media3_ArtefactRemoval_Balloon.avi], which can be found together with all other videos on the CD in Appendix 3. The videos show that the artefact removal is not affected by changing phase offsets in both image acquisition procedures.

As a result of the artefact removal, the vessel wall reveals an almost homogeneous pattern of phase values. Single radial lines are visible, which indicates residual artefacts related to incomplete artefact removal. The results of artefact removal can be seen in the videos [Media4_TissueDoppler_Floating.avi] and [Media5_TissueDoppler_balloon.avi], where Doppler signals inside lumen area have been removed with a mask.

The artefact removal reveals the noise floor in tissue. Regions with high SNR show speckle noise with a speckle size of approximately 10 over 5 pixels. In regions with low SNR, random phase values dominate.

Removal of system artefacts also changes the apparel of the fast moving region in Figure 17 (b). Being characterized by red colours related to a shift towards higher frequencies, this region now appears bigger and shows a circular border. The interpretation of this region is ambiguous and requires a detailed discussion.

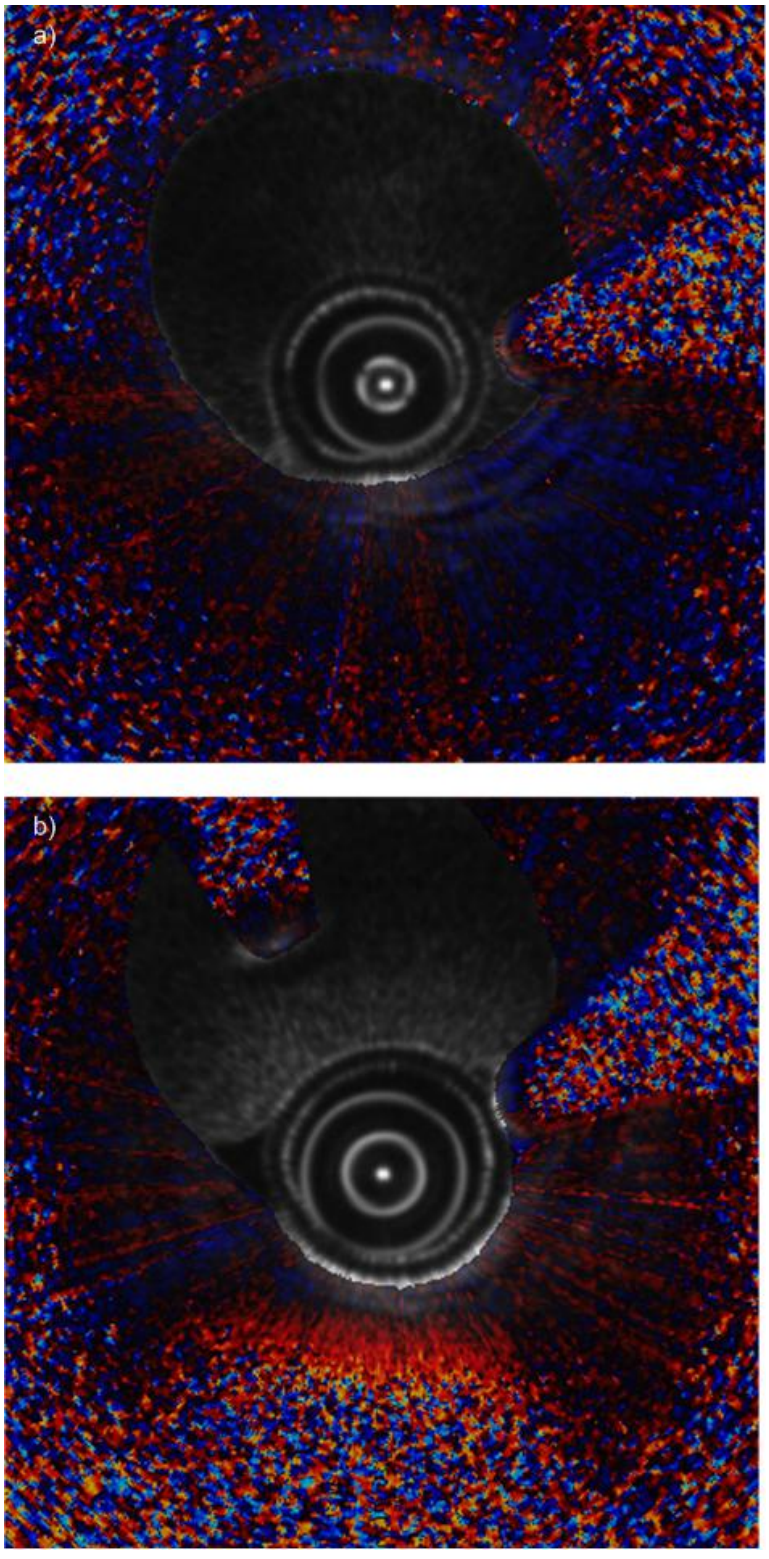

Figure 17: Results of artefact removal

a) without balloon catheterization, b) with balloon catheterization

4. Discussion

Before we are able to discuss the event of this fast moving region we first need to elaborate on some other points, starting with a general view on the presented algorithms to intravascular elastography. The algorithms will be judged on the conclusiveness of their results, based on a comparison with the structural image.

Digital image correlation was performed on structural images that were recorded and preprocessed with corporate software on the C7-XR system. Comparing consecutive frames of a sequence, changes of the thickness of different layers could be identified. Based on this observation, strain should be observed within these layers. The results from DIC presented in this thesis, shows strain as expected. Moreover this, different layers are perceivable in the axial normal strain, which can be explained with variable material properties of these layers.

However using corporate software with unknown noise removal for preprocessing can affect the speckle pattern. Furthermore averaging is included in the transformations related to centering of the lumen. The cross-correlation based results in this thesis thus have to be seen as preliminary results.

Generating results based on raw scan data would improve the results in providing a completely known signal-processing algorithm. Any noise removal included in this algorithm would be required to leave the speckle pattern unchanged, the effects of noise removal on the performance of speckle tracking have never been evaluated to the best of our knowledge.

Despite the alignment, the reconstruction of structural images gives useful results enabling the identification of structural components similar to the findings in preprocessed structural images. Further evaluation regarding noise sources and noise removal in the structural images was not performed, since more effort was put on DOCE.

Particular interest in DOCE was put on analysis and removal of system artefacts induced by unstable imaging conditions in an intravascular setup. Imaging with a free floating catheter, showed phase offsets for complete a-scans, indicating relative movement between tissue and the catheter coupled with the optical fibre. Taping the catheter to a table showed similar results on the catheter sheath. These two observations lead to the assumption that the biggest part of the motion artefact results from rotational movement of the optical fibre and can be estimated from the catheter sheath.

In Figure 17, processed with the current implementation of the algorithm to remove the artefacts, residual radial lines can be seen. This observation indicates that our choice of velocity estimation is not optimum. Faulty estimations can be introduced to this step in various ways.

Given the case of a free-floating imaging catheter, phase offsets can be caused by motion of the tissue. This motion would not be visible on the catheter and thus would not be removed. This kind of error can be evaluated by a comparison of the free floating image acquisition procedure and imaging with a balloon catheter.

By fixing the imaging catheter to a vessel wall with a balloon catheter, a close mechanical coupling between these components could be established. Observing no improvement of the subjective image quality after noise removal, we conclude that relative movement has a minor influence on noise removal.

Another potential source of error is introduced in the manual segmentation. Inaccuracies during the segmentation can include areas outside the catheter, which may have a random phase value. Considering this behaviour, we chose the median for phase estimation, because the median is supposed to be less affected by statistic outliers than the mean value.

Despite these considerations about faulty artefact removal, the algorithm performs well enough to reveal speckle noise, which is generated by scattering at randomly distributed particles [37]. This kind of noise generates a noise floor, limiting the range of velocities that is visible in colour Doppler imaging, as shown in Figure 17.

Within the set of images acquired with colour Doppler imaging, no velocity pattern could be identified that resembles the preliminary results from DIC. This leads to the conclusion that relative velocities are too small to be measured with this system. Observing the change of the thickness of the media confirmed this, revealing a maximum thickness change of ~3 pixels between frames, corresponding to a relative velocity of 45 µm/s and a phase change of 0.01 rad, which is one order of magnitude below the sensitivity of the system, 0.2 rad, as shown in Figure 3 of the publication.

The only Doppler shift pattern within the tissue is visible in sequences recorded with balloon catheterization. The round outline of this region, the flow direction, being reverse to the flow in the artery, and the almost permanent presence over a complete imaging sequence lead to the assumption that this flow pattern belongs to an adjacent vein.

The detection of this blood vessel demonstrates the importance of interpreting colour Doppler images correctly. The current system is able to visualize both blood flow and tissue velocity. Veins and vasa vasorum can appear close to the vessel wall and can lead to an erroneous calculation of strain. It is thus necessary to detect these blood vessels and exclude them from strain calculation.

5. Conclusion

Intravascular OCE is an almost unexplored field of research. This thesis contributes to the research with the development of two new algorithms and their evaluation with an *in vivo* carotid model.

Preliminary results based on DIC showed potential to image strain, including the differentiation of layers, corresponding to layers of different materials in the structural image. This approach shows promising results, given that speckle decorrelation due to various factors can be avoided.

DOCE is a new imaging method to intravascular elastography. As a result of this thesis, an algorithm was developed that is capable of removing system artefacts and revealing movement of blood and tissue. The phase sensitivity after removal of artefacts was evaluated to be 0.2 rad.

Blood flow can have a significant influence on strain distribution. In this thesis, a mixture of saline and blood was imaged with the same algorithm and parallel to DOCE. The results from the *in vivo* model demonstrate the feasibility to image flow velocity as well as flow profile. In addition to this, it was possible to detect adjacent veins, which are an additional influence factor in the distribution of strain.

DOCE has been proven to be difficult using the existing system. Tissue velocities were estimated from structural images and were found to be one order of magnitude below the system sensitivity. Future research is necessary to optimize the system towards better sensitivities.

6. Future Work

The versatile results of this thesis show the potential of Doppler-based intravascular OCE. It can image flow velocity, flow pattern and has the potential to show adjacent blood vessels. Direct elastography however was not possible with the current system.

In order to add this application to the portfolio, the development of a new system is necessary. Multiple approaches are feasible to enable the detection of relative flow patterns: The further reduction of speckle noise and motion artefacts in the imaging system and the development of a fast intravascular loading system.

Another direction of research could be directed towards an optimization of the image processing algorithm. The goals of this approach would be the development of a faster and more precise algorithm to suppress artefacts. These goals could be achieved with an automatic segmentation to detect the catheter sheath and other methods to estimate the optical fibre movement from the phase information in the sheath.

Appendix 1: Description of Matlab Files

Several Matlab-scripts have been created to perform the calculations related to Doppler-based OCE. A short description of these scripts can be found in this appendix. The complete code can be found accompanying the electronic version of this thesis.

Appendix 1a: StructAndCDoppler.m

This script reads the raw signal data from a Doppler OCT system and calculates the structural image and the color Doppler image.

Appendix 1b: GetMasks.m

This script creates a mask for the catheter and one for the lumen area in an intravascular OCT image in Cartesian coordinates. The user is asked to determine these areas with three polygonals, outlining the lumen wall and the inner and outer catheter wall in the structural image. This task is repeated for all frames in apre-defined range. The resulting mask is transformed to polar coordinates and stored in two *.mat file with a user-defined file name and a variable named lumenMask or catheterMask.

Appendix 1c: PhaseUnwrapping.m

This script removes system artefacts from color Doppler images to prepare them for unwrapping. Subsequent to the preparation, quality guided unwrapping is performed.

Appendix 1d: ArtefactRemoval.m

This script removes system artefacts from a color Doppler image. The script is designed for use with a C7-XR OCT system (LightLab). In its current state, the script removes the following artefacts: movement of fibre relative to catheter

The script saves the color Doppler image after removing system artefacts in a *.mat file with the name:

[sequenceName,'cDopplerImage_noArtefacts_polar_raw'].

The script requires the following input values:

- unprocessed color Doppler image
- color Doppler image with unwrapped catheter area
- mask of the catheter area

Appendix 1e: Alignment.m

This script alignes images in a sequence of structural images taken with Ken's software. The rotation is supposed to be an image acquisition or signal processing artefact.

The script saves the structural image and the color Doppler image in polar coordinates after alignment in two *.mat file with the names:

[sequenceName,'cDopplerImage_aligned_polar_raw'],

[sequenceName,'structuralImage_aligned_polar_raw']

The script requires the following input values:

- structural image
- color Doppler image without system artefacts

Appendix 1f: StrainCalculation.m

The script saves the axial displacement image and the axial strain image in polar coordinates in two *.mat file with the names:

[sequenceName,'axialDisplacement_polar_raw'],

[sequenceName,'axialStrain_polar_raw']

The script requires the following input values:

- color Doppler image without system artefacts after alignment
- lumen mask after alignment

Appendix 2: Manuscript of Submitted Publication

In-vivo feasibility of endovascular Doppler optical coherence tomography

Cuiru Sun,[1†] Felix Nolte,[1,2†] Kyle H. Y. Cheng,[1,3] Barry Vuong,[1] Kenneth K.C. Lee,[1,3] Beau A. Standish,[1,2] Brian Courtney,[4] Thomas R. Marotta,[5] Adrian Mariampillai,[1] and Victor X.D. Yang[1,3,5*]

[1]Biophotonics and Bioengineering Laboratory, Dept. Electrical and Computer Engineering, Ryerson University, 350 Victoria St. Toronto ON, M5B2K3 Canada

[2]Faculty of Electrical Engineering and Information Technology, University of Applied Sciences, Karlsruhe, Moltkestraße 30, 76133 Karlsruhe, Germany

[3]Dept. Electrical and Computer Engineering, University of Toronto, 27 King's College Circle, Toronto, Ontario, M5S 1A1, Canada

[4]Colibri Technologies Inc., 3080 Yonge Street, Toronto, ON, Canada M4N 3N1;

[5]Dept. of Medical Imaging, St. Michael's Hospital, 30 Bond Street, Toronto, ON, Canada M5B 1W8;

[†]These authors contributed equally to this work.

*Corresponding author: Victor Yang, MD PhD FRCSC, email: yangv@ee.ryerson.ca

Abstract: Feasibility of detecting intravascular flow using a catheter based endovascular optical coherence tomography (OCT) system is demonstrated in a porcine carotid model *in vivo*. The effects of A-line density, radial distance, signal-to-noise ratio, non-uniform rotational distortion (NURD), phase stability of the swept wavelength laser and interferometer system on Doppler shift detection limit were investigated in stationary and flow phantoms. Techniques for NURD induced phase shift artefact removal were developed by tracking the catheter sheath. Detection of high flow velocity (~ 51 cm/s) present in the porcine carotid artery was obtained by phase unwrapping techniques and compared to numerical simulation, taking into consideration flow profile distortion by the eccentrically positioned imaging catheter. Using diluted blood in saline mixture as clearing agent, simultaneous Doppler OCT imaging of intravascular flow and structural OCT imaging of the carotid artery wall was feasible. To our knowledge, this is the first *in vivo* demonstration of Doppler imaging and absolute measurement of intravascular flow using a rotating fiber catheter in carotid artery.

OCIS codes: (170.4500) Optical coherence tomography; (170.3880) Medical and biological imaging; (280.3340) Laser Doppler velocimetry; (120.5050) Phase measurement

References and links

1. N. Suwanwela, U. Can, K. L. Furie, J. F. Southern, N. R. Macdonald, C. S. Ogilvy, C. J. Hansen, F. S. Buonanno, W. M. Abbott, W. J. Koroshetz, and J. P. Kistler, "Carotid Doppler ultrasound criteria for internal carotid artery stenosis based on residual lumen diameter calculated from en bloc carotid endarterectomy specimens," Stroke **27**, 1965-1969 (1996).
2. A. V. Kamenskiy, Y. A. Dzenis, J. N. MacTaggart, A. S. Desyatova, and I. I. Pipinos, "In vivo three-dimensional blood velocity profile shapes in the human common, internal, and external carotid arteries," Journal of Vascular Surgery **54**, 1011-1020 (2011).
3. J. W. Doucette, P. D. Corl, H. M. Payne, A. E. Flynn, M. Goto, M. Nassi, and J. Segal, "Validation of a Doppler Guide Wire for Intravascular Measurement of Coronary-Artery Flow Velocity," Circulation **85**, 1899-1911 (1992).
4. D. H. Koschyk, C. W. Hamm, and T. Meinertz, "Colour coded blood flow imaging in intravascular ultrasound," Heart **84**, 376-376 (2000).
5. W. G. Li, A. F. W. van der Steen, C. T. Lancee, I. Cespedes, and N. Bom, "Blood flow imaging and volume flow quantitation with intravascular ultrasound," Ultrasound in Medicine and Biology **24**, 203-214 (1998).
6. C. Petersen, D. Adler, and J. Schmitt, "Clinical Studies of Frequency Domain Optical Coherence Tomography in the Coronary Arteries: The First 2000 Patients," Photonic Therapeutics and Diagnostics Vi **7548**(2010).
7. X. Li, T. H. Ko, and J. G. Fujimoto, "Intraluminal fiber-optic Doppler imaging catheter for structural and functional optical coherence tomography," Opt Lett **26**, 1906-1908 (2001).
8. J. A. Izatt, M. D. Kulkami, S. Yazdanfar, J. K. Barton, and A. J. Welch, "In vivo bidirectional color Doppler flow imaging of picoliter blood volumes using optical coherence tomograghy," Optics Letters **22**, 1439-1441 (1997).
9. H. Ren, Z. Ding, Y. Zhao, J. Miao, J. S. Nelson, and Z. Chen, "Phase-resolved functional optical coherence tomography: simultaneous imaging of in situ tissue structure, blood flow velocity, standard deviation, birefringence, and Stokes vectors in human skin," Opt Lett **27**, 1702-1704 (2002).
10. B. J. Vakoc, S. H. Yun, J. F. de Boer, G. J. Tearney, and B. E. Bouma, "Phase-resolved optical frequency domain imaging," Optics Express **13**, 5483-5493 (2005).

11. A. M. Rollins, S. Yazdanfar, R. Ung-Arunyawee, and J. A. Izatt, "Real time color Doppler optical coherence tomography using a novel autocorrelation technique," in *Lasers and Electro-Optics, 1999. CLEO '99. Summaries of Papers Presented at the Conference on*, 1999), 451-452.
12. V. X. D. Yang, M. L. Gordon, A. Mok, Y. Zhao, Z. Chen, R. S. C. Cobbold, B. C. Wilson, and I. Alex Vitkin, "Improved phase-resolved optical Doppler tomography using the Kasai velocity estimator and histogram segmentation," Optics Communications **208**, 209-214 (2002).
13. K. H. Y. Cheng, C. R. Sun, J. P. Cruz, T. R. Marotta, J. Spears, W. J. Montanera, P. R. Herman, A. Thind, B. Courtney, B. A. Standish, and V. X. D. Yang, "Feasibility of endovascular optical coherence tomography for high-resolution carotid vessel wall imaging," Photonic Therapeutics and Diagnostics Viii, Pts 1 and 2 **8207**(2012).
14. K. H. Cheng, C. Sun, J. P. Cruz, T. R. Marotta, J. Spears, W. J. Montanera, A. Thind, B. Courtney, B. A. Standish, and V. X. Yang, "Comprehensive data visualization for high resolution endovascular carotid arterial wall imaging," J Biomed Opt **17**, 056003 (2012).
15. V. X. D. Yang, M. L. Gordon, B. Qi, J. Pekar, S. Lo, E. Seng-Yue, A. Mok, B. C. Wilson, and I. A. Vitkin, "High speed, wide velocity dynamic range Doppler optical coherence tomography (Part I): System design, signal processing, and performance," Optics Express **11**, 794-809 (2003).
16. Kenneth K. C. Lee, Adrian Mariampillai, Joe X. Z. Yu, David W. Cadotte, Brian C. Wilson, Beau A. Standish, and V. X. D. Yang, "Real-time speckle variance swept-source optical coherence tomography using a graphics processing unit," Biomed. Opt. Express **3**, 1557-1564 (2012).
17. D. J. Smithies, T. Lindmo, Z. P. Chen, J. S. Nelson, and T. E. Milner, "Signal attenuation and localization in optical coherence tomography studied by Monte Carlo simulation," Phys Med Biol **43**, 3025-3044 (1998).
18. G. van Soest, J. G. Bosch, and A. F. W. van der Steen, "Azimuthal registration of image sequences affected by nonuniform rotation distortion," IEEE Trans. Info. Tech. Bio. Med. **12**, 348-355 (2008).
19. G. J. Tearney, E. Regar, T. Akasaka, T. Adriaenssens, P. Barlis, H. G. Bezerra, B. Bouma, N. Bruining, J. M. Cho, S. Chowdhary, M. A. Costa, R. de Silva, J. Dijkstra, C. Di Mario, D. Dudeck, E. Falk, M. D. Feldman, P. Fitzgerald, H. Garcia, N. Gonzalo, J. F. Granada, G. Guagliumi, N. R. Holm, Y. Honda, F. Ikeno, M. Kawasaki, J. Kochman, L. Koltowski, T. Kubo, T. Kume, H. Kyono, C. C. S. Lam, G. Lamouche, D. P. Lee, M. B. Leon, A. Maehara, O. Manfrini, G. S. Mintz, K. Mizuno, M. A. Morel, S. Nadkarni, H. Okura, H. Otake, A. Pietrasik, F. Prati, L. Raber, M. D. Radu, J. Rieber, M. Riga, A. Rollins, M. Rosenberg, V. Sirbu, P. W. J. C. Serruys, K. Shimada, T. Shinke, J. Shite, E. Siegel, S. Sonada, M. Suter, S. Takarada, A. Tanaka, M. Terashima, T. Troels, S. Uemura, G. J. Ughi, H. M. M. van Beusekom, A. F. W. van der Steen, G. A. van Es, G. van Soest, R. Virmani, S. Waxman, N. J. Weissman, and G. Weisz, "Consensus Standards for Acquisition, Measurement, and Reporting of Intravascular Optical Coherence Tomography Studies A Report From the International Working Group for Intravascular Optical Coherence Tomography Standardization and Validation," Journal of the American College of Cardiology **59**, 1058-1072 (2012).
20. K. H. Y. Cheng, C. Sun, B. Vuong, K. K. C. Lee, A. Mariampillai, T. R. Marotta, J. Spears, W. J. Montanera, P. R. Herman, T. R. Kiehl, B. A. Standish, and V. X. D. Yang, "Endovascular optical coherence tomography intensity kurtosis: visualization of vasa vasorum in porcine carotid artery," Biomedical Optics Express **3**, 388-399 (2012).
21. Dennis C. Ghiglia and M. D. Pritt, *Two-Dimensional Phase Unwrapping: Theory, Algorithms and Software* (Wiley-Interscience, New York, 1998).
22. R. S. C. Cobbold, *Foundations of biomedical ultrasound* (Oxford University Press, Oxford, 2007), p. 832.
23. S. G. Proskurin, I. A. Sokolova, and R. K. Wang, "Imaging of non-parabolic velocity profiles in converging flow with optical coherence tomography," Phys Med Biol **48**, 2907-2918 (2003).
24. B. Rao, L. F. Yu, H. K. Chiang, L. C. Zacharias, R. M. Kurtz, B. D. Kuppermann, and Z. P. Chen, "Imaging pulsatile retinal blood flow in human eye," Journal of Biomedical Optics **13**(2008).
25. Darren Morofke, Michael C. Kolios, I. Alex Vitkin, and Victor X. D. Yang, "Wide dynamic range detection of bidirectional flow in Doppler optical coherence tomography using a two-dimensional Kasai estimator," Opt. Lett. **32**, 253-255 (2007)
26. J. Kalkman, A. V. Bykov, G. J. Streekstra, and T. G. van Leeuwen, "Multiple scattering effects in Doppler optical coherence tomography of flowing blood," Phys Med Biol **57**, 1907-1917 (2012).
27. F. J. H. Gijsen, J. J. Wentzel, A. Thury, F. Mastik, J. A. Schaar, J. C. H. Schuurbiers, C. J. Slager, W. J. van der Giessen, P. J. de Feyter, A. F. W. van der Steen, and P. W. Serruys, "Strain distribution over plaques in human coronary arteries relates to shear stress," Am J Physiol-Heart C **295**, H1608-H1614 (2008).

1. Introduction

Blood flow velocity and volumetric flow measurements are important parameters for assessment of the severity of stenosis and the outcome of interventional therapy. Over the last two decades Duplex ultrasonography [1, 2] has become a routine imaging and measurement technique for the detection and clinical monitoring of carotid stenosis. Despite the inherent alteration of hemodynamics as a consequence of physically placing a catheter in the coronary artery, intravascular ultrasound Doppler measurements [3] have been used for coronary blood flow measurements. Other ultrasound techniques such as color coded intravascular ultrasound blood flow imaging [4] and de-correlation based flow measurements [5] have been proposed to extract flow information from cross-sectional IVUS data and display simultaneous morphological data and flow information. Endovascular optical coherence tomography (OCT) has become an important modality for coronary stenosis imaging and stenting evaluation [6]. However, limited *in vivo* blood flow measurement has been conducted by endovascular OCT since the attempt by Li. *et al* [7] to measure the intraluminal velocity profile in a vessel phantom using a prototype OCT Doppler catheter. Using color Doppler [8], phase-resolved Doppler OCT [9, 10], autocorrelation [11] or

Kasai velocity estimation techniques [12] in a circumferentially scanning catheter probe carries it's unique challenges. These include dilution of blood by saline to improve OCT penetration, motion artefacts induced by the rotating optical probe, and the radially dependent noise background of measured Doppler signals. The widespread clinical use of the C7-XR OCT system (Lightlab Imaging, St. Jude Medical Inc. St. Paul, Minnesota, USA) would benefit from a technique compatible with rotational OCT catheters for Doppler imaging. In this paper we show preliminary results of *in vivo* intraluminal blood flow measurement using endovascular OCT in a porcine carotid model.

2. Materials and methods

Porcine carotid imaging protocols were approved by the Animal Care Committees of Sunnybrook Health Sciences Centre and St. Michael's Hospital, Toronto, Ontario, Canada, and described previously [13,14]. We noted the C7-XR OCT system has been applied to various endovascular structural imaging successfully with its high frame rate of 100 frames/s. However with ~500 A-scans in each frame, there is little overlap for adjacent pixels and thus the real-time velocity estimation by phase resolved methods could not be obtained accurately [15]. A custom-made data acquisition system [16] was combined with the C7-XR OCT system to acquire high-density A-line images at 20 frames/s rates that are suitable for Doppler shift calculation.

2.1 System configuration

The system used in this study consists of the C7-XR OCT system and a personal computer equipped with a data acquisition card (ATS9350, Alazartech) via PCIe x8 interface, a display card with graphics processing unit (GPU) for high speed computation (GeForce GTX 460 1GB, NVIDIA) over PCIe x16 interface and a solid state drive (Intel 510 Series 250GB) through SATA II interface. Figure 1 (a) displays the interconnections between the hardware and the motherboard, and the connection between the personal computer and the back end of the C7-XR OCT system, which enabled raw OCT signal acquisition, saving and post-processing. The DAQ channels included a linear *k*-clock, the A-scan trigger, and the raw OCT signal. Previously developed custom-built software [16] was employed in this study with addition of minor modifications to accommodate the endovascular OCT system that provided a linear *k*-space sampling clock.

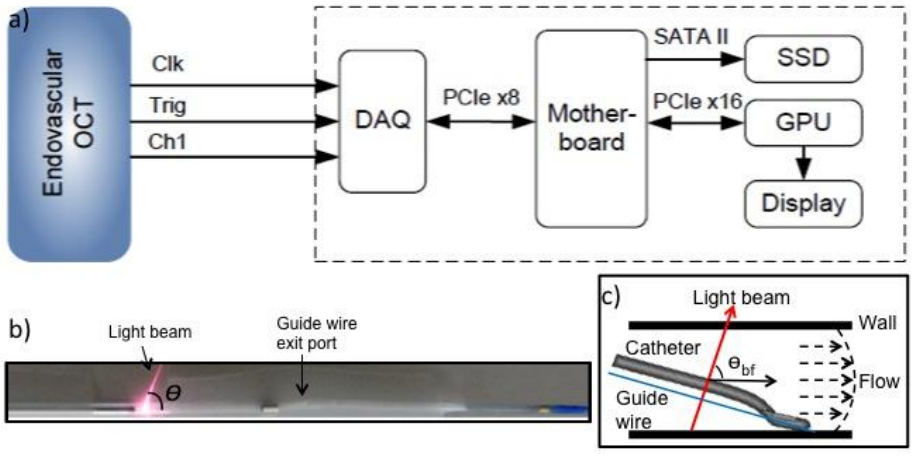

Fig. 1

Fig. 1. Doppler imaging setup for endovascular OCT system. (a) High-speed data acquisition and graphics processing unit (GPU) processor connection to back end of C7-XR OCT system for high density A-line imaging. Clk: *k*-clock, Trig: A-scan trigger, Ch1: channel for raw OCT signal; DAQ: data acquisition; SSD: solid-state drive. (b) The imaging catheter showing the Doppler angle of the imaging beam, which is variable depending on the position of the guide wire and catheter location. (c) A schematic diagram showing the imaging catheter is not coaxial with the blood vessel. θ_{bf} indicates the beam-to-flow angle.

The angle between the scanning beam and the axis of catheter (C7 Dragonfly, St. Jude Medical Inc. St. Paul, Minnesota, USA) was measured to be ~70° in air without water or saline injection from a measurement shown in Fig. 1 (b). However, this angle may change slightly during imaging due to refractive index variation of various mixing ratios of water, blood, contrast and saline. Moreover, in most cases, the imaging catheter is not coaxial with the blood vessel, as determined by the positions of the guide wire and image catheter. This non-coaxial orientation (shown in Fig. 1 (c)) while in most cases creates non-perpendicularity between the beam and flow direction such that the Doppler signal induced by blood flow can be obtained also represents a source of error in determining the absolute flow velocity.

The flow velocity is calculated from Doppler shift obtained by Kasai autocorrelation [15]. The resulting measurement accuracy of blood flow depends on the size of the window used for Kasai calculation and the percentage of voxel overlap between adjacent A-lines. To optimize the radial and circumferential resolution, the percentage of overlap of the window is carefully chosen based on the axial point spread function (PSF) and spot size of the OCT system. The axial PSF at 3 dB is ~ 14 um in air, resulting in ~ 10 um in tissue, which degrades due to multiple scattering of photons and dispersion. However, previous research has shown that the variation of PSF remains minimal within blood vessels, for example, approximately 4% at an optical depth of 35 mean free path (mfp) [17]. The spot size and working distance (from the edge of the catheter) of the catheter are 25 um and ~1.5 mm respectively. The scanning beam diverges as the distance from the catheter is increased as shown in Fig. 2 (a). The percentage of overlap of adjacent voxels according to the beam spots is plotted in Fig. 2 (b). The two curves representing percentage of voxel overlap versus the distance from the catheter for 500 A-lines/frame and 2500 A-lines/frame respectively. It can be seen that the pixels still have ~80% overlap at 4 mm away from the catheter at 2500 A-lines/frame, while the overlap percentage drops dramatically for 500 A-lines/frame. Therefore 2500 A-line/frame images would be more suitable for accurate Doppler shift calculations. A 2×10 window (at depth and transverse directions relative to the optical beam) was chosen for Kasai autocorrelation calculation of Doppler shift to improve velocity detection sensitivity during Doppler processing.

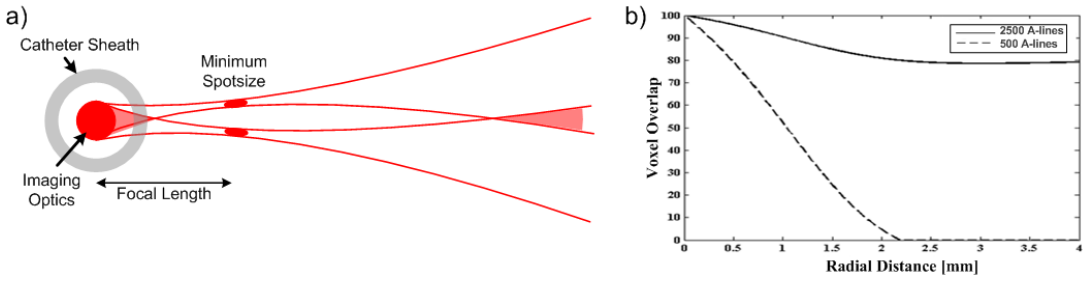

Fig. 2. (a) A schematic diagram showing the scanning beam from the imaging catheter. (b) Percentage of voxel overlap changes with the distance from the catheter for 2500 A-lines and 500 A-lines per frame. The rapid decline of voxel overlap between A-lines for the latter condition limits adequate imaging of Doppler shift.

2.2 Motion artefact of imaging catheter removal

Movement of the catheter induces artefact, which can be observed from the Doppler image of the sheath of the catheter. The rotation and axial motion of the fiber optic core within the catheter during endovascular imaging procedure also contribute to the detected Doppler image artefacts, and limit the minimal detectable velocity. Bending and twisting of the imaging catheter sheath, unavoidable during *in vivo* navigation of the catheter through the vasculature, can adversely couple with the high speed rotation of the optic fiber and induce vibration. The vibration can introduce undesired relative motion (both radial and longitudinal) between the optic fiber and the catheter sheath. The resultant non-uniform rotational distortion (NURD) [18], when severe, can induce obvious artefacts in the structural imaging [19]. Phase sensitive imaging is more susceptible to such relative motion and significant phase shift artefact can exist without obvious structural imaging NURD.

To understand the NURD induced phase shift artefacts caused by the complex fiber motion and its effect on flow detection, a slow flow phantom was imaged with the Dragonfly catheter. Homogenously diluted mixture of blood (1.5% by volume) in saline, simulating imcompletely clearing of blood during saline flush, was injected to the flow phantom at 50 ml/hr (corresponding to 3.5 mm/s maximal flow velocity) using an infusion pump. The imaging results are shown in Fig. 3. (a) is a structural image, from which the sheath and internal reflection of the imaging catheter can be observed. The catheter sheath, containing inner and outer surface reflections, can serve as reference surfaces for phase shift calibration against the phase artefacts. In addition, internal multiple reflection, such as those from the interface of focal elements in the fiber probe, may serve as phase shift calibration against phase instability in the swept source laser, interferometer and DAQ of the OCT system. The Doppler shift generated in the internal reflection (shown in Fig. 3 (b)) is < 0.02 rad, therefore the phase instability induced error is negligible. Without removing the NURD induced phase artefacts, the slow flow rate induced Doppler shift is completely masked as shown in Fig. 3 (c). The total Doppler shift detected in the flow region is a vector sum of the shift generated by the flowing particles and the shift produced by the moving fiber optic. From Fig. 3 (c), it can be seen that the bulk-phase change induced by the oscillation of the fiber optic is constant along the radial direction. Therefore the fiber motion artefact can be eliminated by subtracting the Doppler shift measured on the sheath of the catheter. The corrected phase map is shown in Fig. 3 (d), where the average Doppler shift of the flow is ~ 0.4 rad corresponding to flow velocity of 4 mm/s, which is comparable with the theorectical value.

2.3 Noise floor in Doppler shift measurement

During endovascular imaging, except for various motion artefacts, the density of A-lines and the angular line spaces increasing along the radius would also affect the Doppler shift calculation. A phantom was constructed to evaluate these effects. The phantom was made of

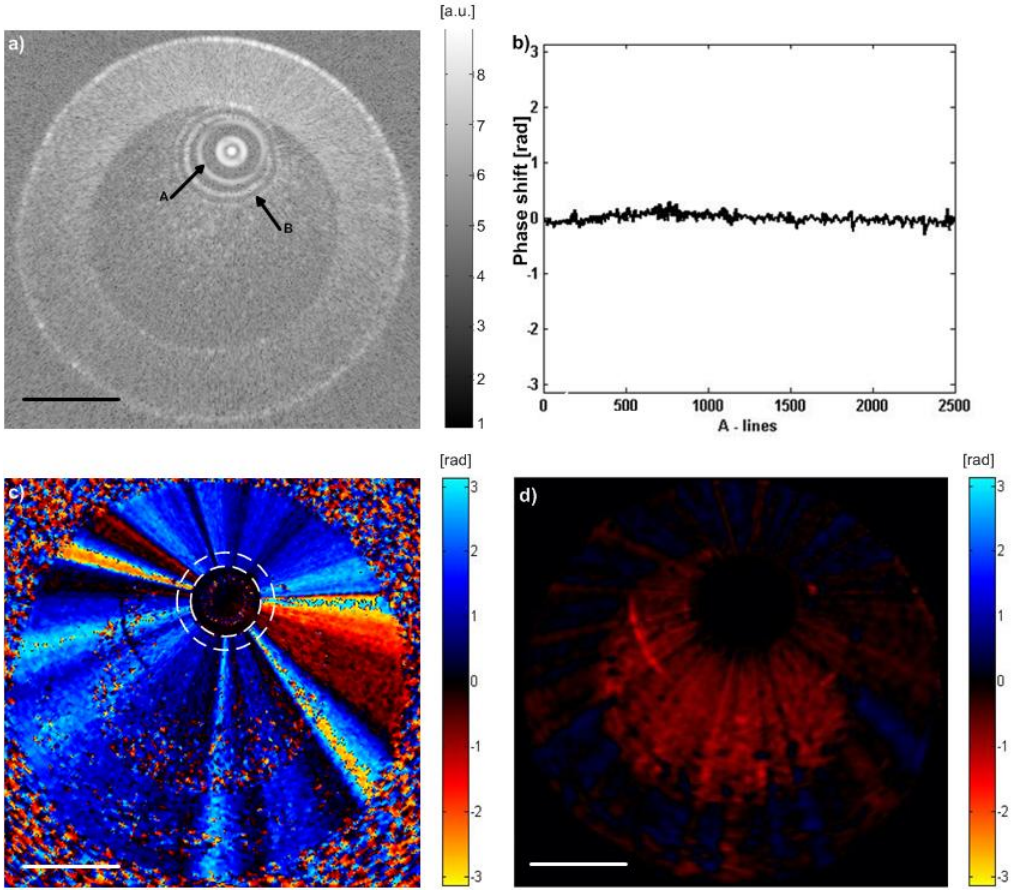

Fig.3 Imaging of a slow flow phantom. (a) Structural image of 1.5% blood in saline mixtrue within the tube, where arrow A indicates the internal reflection of the imaging optics, and arrow B indicates the outer surface of the imaging catheter sheath. (b) Phase shift obtained from the internal reflecton indicated by arrow A. (c) Doppler shift image of the slow flow phantom. The dashed ring indicates the sheath of the imaging catheter, with phase shift induced by NURD in a radially constant manner throughout the image. (d) Doppler image after supression of the motion artefact, which displays the phase shift induced by the slow flow inside the tube phantom. Scale bars = 1 mm.

gelatin with TiO_2 particles to model scatterers (concentration: 0.5 g/l). The concentration of TiO_2 was chosen to simulate relatively low SNR conditions that would be encountered during *in-vivo* endovascular imaging, with incomplete clearing of blood in the vessel lumen. A tube with ~3 mm outer diameter was embedded to allow insertion of the OCT catheter. The Dragonfly OCT imaging catheter was advanced in the tube through a guide wire to the region of interest. Since there is no movement of the phantom, any nonzero phase shift detected during this procedure was attributed to measurement error. A cross-section of the phantom was imaged by both 2500 A-lines per frame and 500 A-lines per frame. Figure 4 (a) and (b) demonstrate the structural and color Doppler images after removing bulk motion induced by catheter oscillation. Both images were acquired with 2500 A-lines per frame. The white sector in (a) indicates a region of interest (ROI), where the Doppler shift was calculated as shown in (b). The standard deviation of the phase shift determines the minimal detectable phase change. This parameter varies with the radial distance and signal to noise ratio (SNR) of the OCT signal. Figure 4 (c) and (d) show these relations for 2500 A-line per frame mode, and in comparison, 500 A-line per frame mode. The latter showed consistently higher noise floor in the phase measurement, and would not be suitable for *in-vivo* measurements. When the radial distance from the catheter increases or when the SNR decreases, the phase measurement noise floor increases as expected [10].

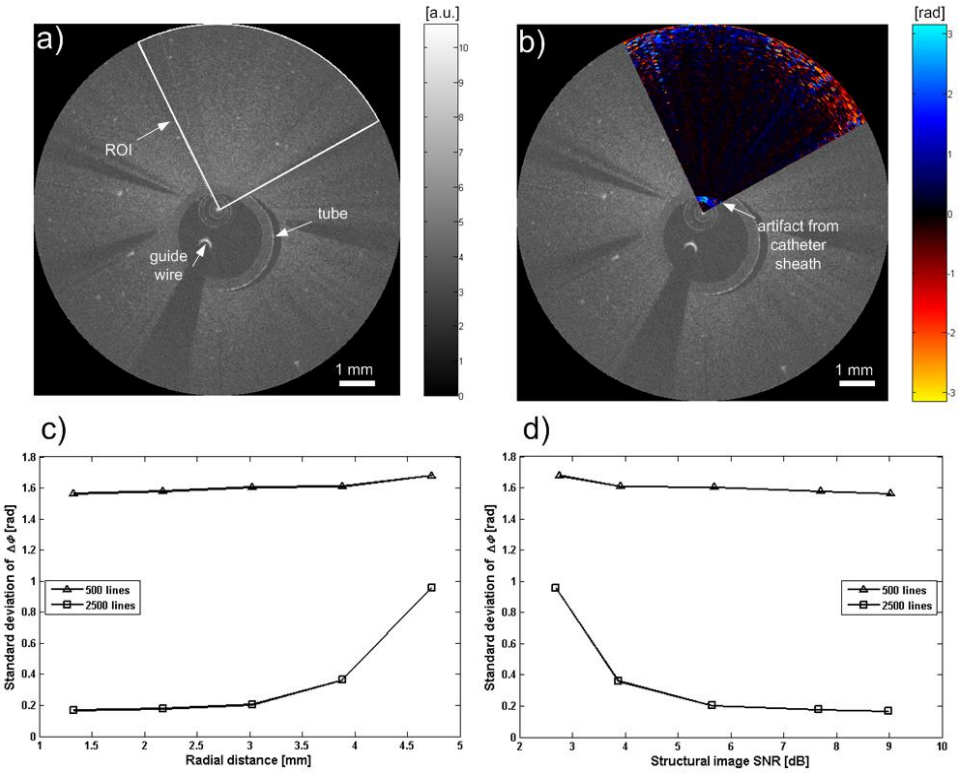

Fig. 4. (a) Structural image of a stationary tissue phantom with TiO_2 particles. White sector represents the ROI. (b) Color Doppler image of the ROI after bulk motion correction. (c) The standard deviation of the Doppler shift changes with radial distance and (d) signal to noise ratio (SNR). The data points in (c) and (d) represent five regions at different radial distances, consisting of 39,600 pixels (2500 A-lines per frame) or 7,920 pixels (500 A-lines per frame). The low SNR phantom is constructed to mimic low SNR of intraluminal blood typically encountered during in-vivo experiments. The Doppler noise floor increases at the edge of the image with larger radial distance (less voxel overlap between A-lines) and lower SNR.

3. *In vivo* porcine carotid artery imaging

Intravascular flow velocity profiles in porcine carotid arteries were imaged *in vivo* using the above system setup. The *in vivo* porcine carotid imaging procedure presented in this paper has been previously described by our group [20] after adaptation of using 1.5% by volume blood in saline mixture instead of pure saline as the clearing agent injected by an automated pump during Doppler OCT imaging. Briefly a femoral incision was made at the groin of the pig, which was continuously anaesthetized. An 8-French catheter was inserted into the incision as the entry point of the catheter system. Various catheters were used to aid the final insertion of the guide wire and OCT imaging catheter to the carotid artery. Doppler OCT images consisting of 2500 A-lines/frame were taken at a frame rate of 20 frames/s without pullback.

A 3-dimensional reconstruction from pull-back OCT imaging may help to deduce the angle between the catheter axis and the vessel center-line, which may help with better estimation of the beam to flow angle. Structural images of the vessel wall were first obtained by flushing the blood with pure saline. A 3D structural image of the vessel with catheter and guide wire inside are shown in Fig. 5 (a), which shows the catheter is at approximately 10° angle with the vessel wall. The insertion of a catheter into an artery leads to the formation of an annular region between the catheter wall and the arterial wall. A comparison is made with finite element simulation of eccentric annular flow. The simulation is carried out with incompressible and Newtonian fluid with density of 1060 kg/m^3 and viscosity of 0.003 Pa·s. Simulation

geometry is set with vessel diameter of 2.5 mm, catheter diameter 0.9 mm, and established laminar flow pattern. The catheter is positioned eccentrically with a gap of 0.2 mm from the vessel wall. The volumetric flow rate applied at the inlet was 5 ml/s, similar to typical saline flush injection rate used for the porcine experiments. The flow profile obtained from the simulation is shown in Fig. 5 (b), where the maximum flow is ~ 57 cm/s.

At the end of flushing when the blood flow mixed with saline images of 500 A-lines/frame and 2500 A-lines/frame were both recorded for Doppler flow measurement. One frame of the structural OCT image of porcine carotid artery consisting of 2500 A-lines is shown in Fig 5 (c). A seam line appear at the location of the transition between the first and the last A-line due to changes in vessel dimension and relative catheter motion during a cardiac cycle [20]. The longer arrow denotes the guide wire and its artefact. The same cross section imaged by 500 A-lines/frame overlaid with the Doppler signal is shown in Fig. 5 (d), where the Doppler shift image shows mainly noise, as expected. In comparison, Fig. 5 (e), (f) and (g) show the 2500 A-lines images, without Doppler artefact removal, with removal, and after applying structural mask to show only the intravascular flow Doppler shift. Due to the high flow velocity in the carotid vessel, the Doppler shift is aliased between $[-\pi, \pi]$. The aliasing pattern within the vessel lumen is distorted by the NURD induced phase artefacts, introducing significant asymmetry in the phase image, as shown in Fig. 5 (e). Correction of the phase artefacts, by tracking the phase shift observed on the catheter sheath, significantly reduces the distortion and returns the aliasing contour lines towards the expected pattern. The NURD induced phase artefacts are time variant as shown by video [Media 1_Fig_5_e_f.AVI] and therefore, frame to frame subtraction will not be sufficient. There are residual phase artefacts which may be greater than those induced by vessel wall motion secondary to arterial pulsation.

A quality-guided phase unwrapping algorithm [21] was used to unwrap the phase map and the corresponding unwrapped phase map is shown in Fig. 5 (h). The maximum Doppler shift indicated by '*' is ~ 24 rad, representing highest blood flow velocity of ~ 51 cm/s calculated with an estimated Doppler angle of 80°. The arrow indicated area was not unwrapped correctly due to the high shear rate near the wall and Doppler shift noise, which can be observed in (g). The area between the guide wire and the seam line could not be unwrapped properly due to the discontinuity induced by the motion of the catheter and the guide wire. Therefore, this region was not displayed in Figure 5 (h).

In certain clinical settings, it may not be required to phase unwrap the Doppler image, as the aliasing provides natural contour plot of the flow profile. Fig. 6 demonstrates a video of simultaneous structural and Doppler OCT imaging of a porcine carotid artery, where dilute (1.5%) blood in saline flush is injected with a contrast injector pump at 5 ml/s (note: typical human carotid angiography uses 4 to 6 ml/s injection rate of contrast). Structural OCT NURD effects can be seen at the 6 to 7 o'clock sector. Seam lines can be seen at 11 to 2 o'clock sector in the Doppler flow images. At the beginning of the video sequence, there is homogenous filling of the vessel lumen by the blood in saline flush, while the vessel wall is still visible. Despite the dilute nature of the flush (1.5% blood by volume), Doppler shift induced by the intravascular flow is clearly visible with associated aliasing rings, which shows the changes of flow waves with time due to changes of injection rate (velocity) [22]. Visibility of the carotid artery wall is affected towards the end of the video sequence, when the injection comes to an end and increased amount of blood starts to fill in the lumen.

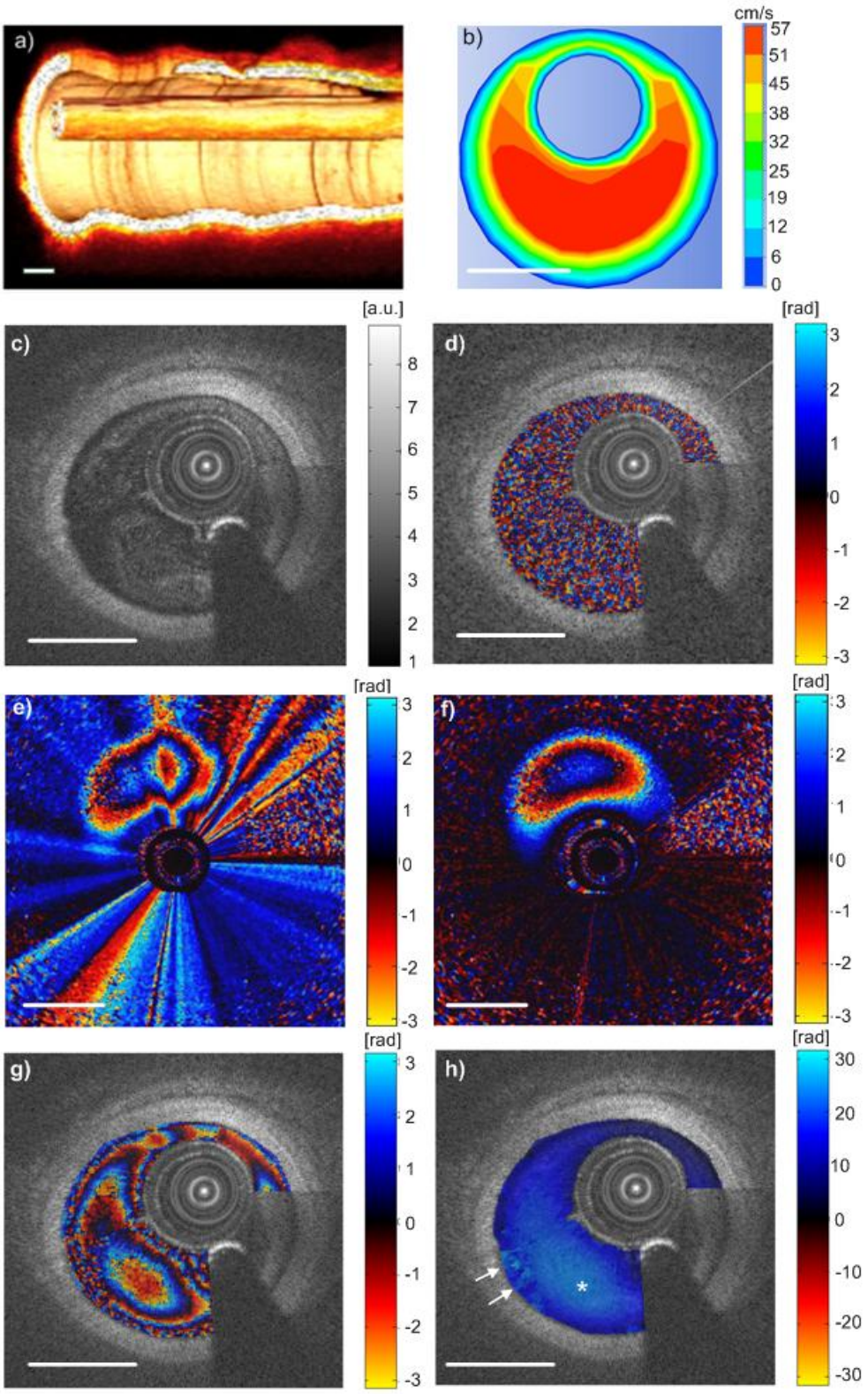
a)
b)
cm/s
57
51
45
38
32
25
19
12
6
0
c)
[a.u.]
8
7
6
5
4
3
2
1
d)
[rad]
3
2
1
0
-1
-2
-3
e)
[rad]
f)
[rad]
g)
[rad]
h)
[rad]
30
20
10
0
-10
-20
-30

Fig. 5

Fig. 5 *In vivo* endovascular flow measurement. (a) 3D OCT image of the catheter and the vessel wall, which shows the angle between the catheter and the wall is ~10°. (b) Simulation results of blood flow. (c) Cross-sectional OCT image of a porcine carotid artery with shadow casted by guide wire. (d) The same cross-section as (c) imaged by 500 A-lines/frame with Doppler shift overlaid, showing mainly noise. (e) and (f) (Media 1). (e) Phase shift image, 2500 A-lines/frame, without NURD induced phase artefact removal. It shows distorted phase contour lines. (f) Phase shift image after NURD induced phase artefact removal by tracking the phase shift in the catheter sheath. The corrected phase contour lines are as expected. The NURD induced artefact is time variant, as shown by video [Media 1_Fig_5_e_f.AVI] [In this thesis, the video can be found in Appendix 3] (g) A typical cross-sectional frame, 2500 A-lines/frame with Doppler shift overlaid, showing aliased phase changes. (h) The unwrapped phase map of (g), where * indicates the highest velocity region. The arrows indicate incorrect phase unwrapping due to noise and high shear rate near the vessel wall. Scale bars = 1 mm

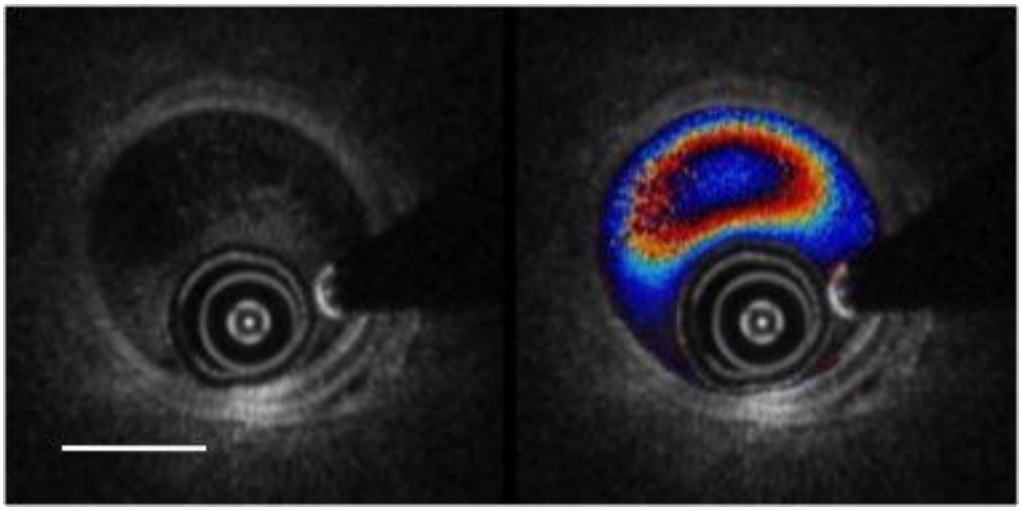

Fig. 6. (Media 2) Simultaneous structural (left) and Doppler overlay (right) OCT video [Video_Fig_6.AVI] [Name changed in thesis: Media2_Fig_6.avi, Video can be found in Appendix 3] images over 2 seconds during the late phase of pump injection. Note the arterial pulsations in the structural images and the aliasing rings of the flow profile in the Doppler image. A seam line is moving through between the 11 o'clock and 2 o'clock positions, more apparent in the Doppler image than the structural. Scale bar = 1 mm.

4. Discussion and conclusion

While multiple different scanning protocols for phase resolved Doppler OCT flow imaging in the Cartesian coordinate have been introduced in the recent years [23, 24], especially with the advance of increased A-scan rates available via high speed swept wavelength lasers or line-scan cameras and galvoscanners, rotational catheter based phase resolved Doppler OCT for intravascular flow is less developed. Frame to frame phase shift calculation is not reliable with fiber rotational speed of 100 rps during *in vivo* imaging. Therefore, line-to-line phase calculation needs to be employed, yet 50 to 100 kHz A-scan rate limits the frame rate since sufficient A-scan density is required for Doppler imaging, as demonstrated in this work.

Currently the minimum detectable flow velocity determined by the noise floor of the Doppler shift shown in Fig. 3 a) is ~ 2 mm/s, assuming a Doppler angle of 70º. The maximum detectable velocity, when multiple aliasing rings are visible, is affected by a combination of factors including SNR, spatial resolution, and the performance of the phase unwrapping techniques. In principle, phase unwrapping technique breaks down when the velocity gradient equivalent to 2π occurs over a spatial dimension comparable to the resolution of the OCT system [25]. In practice, reduced SNR due to the low scattering

flush fluid (1.5% blood in saline) will further decrease the maximal detectable velocity. The finite element simulation provided similar results with real-time intravascular imaging as shown in Fig. 5, demonstrating measurement of absolute flow velocity at 51 cm/s.

We note the simulation contains assumptions including non-deformable straight tube with homogenous material properties, fluid density and viscosity of blood. These depart from biological tissue with visco-elastic properties and responds to pressure wave propagation from the arterial pulse. Many other factors, such as scatterer concentration and tissue scattering parameters [26] affect the OCT signal and Doppler flow profile measurement. The main source of error, however, arises from inability to precisely define the Doppler angle in this work. Under *in-vivo* conditions with catheter bending within pulsating vessel, 10º angular error will not be an over estimation as observed from real-time angiography. Therefore, future Doppler measurement accuracy improvement can be obtained by conical rotational scanning.

In comparison to IVUS based Doppler methods for intravascular flow imaging, Doppler OCT provides better spatial and velocity resolution as both technique are subjected to the same Doppler angle error, but optical wavelength is much shorter than IVUS even when the latter operates at 100 MHz. OCT suffers from the need to optically clear the blood while imaging, hence the pump injector may distort the intravascular flow profile from physiological states. We note, however, during most catheter based interventional procedures, the multiple devices inside the vessel (e.g., guide catheter, imaging catheter, guide wires, etc.) would have already significantly altered the flow profile. Directly imaging changes during different stages of interventional treatment, such as those before and after angioplasty or stenting, will provide insights to clinical applications, especially considering subtle changes of the vessel in geometry can affect the flow field significantly [27].

In conclusion, simultaneous structure OCT imaging and Doppler flow measurement in porcine carotid artery was demonstrated, after investigating the required A-scan density and NURD induced phase shift artefact. Using an endovascular OCT system with custom-built data acquisition system and phase shift artefact removal algorithm, minimal detectable velocity was characterized in a slow flow phantom. To our knowledge, this is the first *in vivo* demonstration of Doppler imaging and absolute measurement of intravascular flow using a rotating fiber catheter in carotid artery.

Acknowledgement

This work was supported by the Canadian Institutes of Health Research (CIHR), the Natural Sciences and Engineering Research Council of Canada (NSERC), Ontario Brain Institute, Ryerson University, Canada Research Chair (CRC) and German Academic Exchange Service (DAAD).

Appendix 3: Electronic Version of Supplemental Material

Bibliography

[1] D. D. Nolte, "Optical Coherence Tomography," in *Optical Interferometry for Bioogy and Medicine*, ed, 2011.

[2] F. S. Foster*, et al.*, "Advances in ultrasound biomicroscopy," *Ultrasound in Medicine and Biology,* vol. 26, p. 27, 2000.

[3] M. J. Thali*, et al.*, "Is 'virtual histology' the next step after the 'virtual autopsy'? Magnetic resonance microscopy in forensic medicine," *Magnetic Resonance Imaging,* vol. 22, p. 8, 2004.

[4] J. M. Schmitt, "OCT elastography: imaging microscopic deformation and strain of tissue," *Optics Express,* vol. 3, p. 13, 1998.

[5] D. D. Duncan and S. J. Kirkpatrick, "Processing algorithms for tracking speckle shifts in optical elastography of biological tissues," *Journal of Biomedical Optics,* vol. 6, pp. 418 - 426, 2001.

[6] H.-J. Ko*, et al.*, "Opical coherence elastography of engineered and developing tissue," *Tissue Engineering,* vol. 12, pp. 63 - 73, 2006.

[7] J. Rogowska*, et al.*, "Optical coherence tomographic elastography technique for measuring deformation and strain of atherosclerotic tissues," *Heart,* vol. 90, pp. 556-562, 2004.

[8] S. J. Kirkpatrick*, et al.*, "OCT-based elastography for large and small deformations," *Optics Express,* vol. 14, pp. 11585 - 11597, 2006.

[9] X. Liang*, et al.*, "Optical micro-scale mapping of dynamic biomechanical tissue," *Optics Express,* vol. 16, pp. 11052 - 11065, 2008.

[10] X. Liang*, et al.*, "Modeling and measurement of tissue elastic moduli using optical coherence elastography," in *Optics in Tissue Engineering and Regenerative Medicine II (SPIE)*, 2008, pp. 685803-1 - 685803-8.

[11] X. Liang and S. A. Boppart, "Dynamic optical coherence elastography and applications," in *Optical Sensors and Biophotonics (SPIE-OSA-IEEE)*, 2009, pp. 763403-1 - 763403-6.

[12] S. G. Adie*, et al.*, "Audio frequency *in vivo* optical coherence elastography," *Physics in Medicine and Biology,* vol. 54, pp. 3129 - 3139, 2009.

[13] C. L. de Korte and A. F. W. van der Steen, "Intravascular Ultrasound Elastography: An Overiew," *Ultrasonics,* pp. 859-865, 2002.

[14] H. E. Talhami*, et al.*, "Spectral Tissue Strain: A New Technique for Imaging Tissue Strain using Intravascular Ultrasound," *Ultrasound in Medicine & Biology,* vol. 8, pp. 759-772, 1994.

[15] L. K. Ryan and F. S. Foster, "Ultrasonic measurement of differential displacement and strain in a vascular model," *Ultrasonic Imaging,* vol. 19, pp. 19 - 38, 1997.

[16] B. M. Shapo*, et al.*, "Displacement and Strain Imaging of Coronary Arteries with Intraluminal Ultrasound," *IEEE Transactions on Ultrasonics, Ferroelectrics and Frequency Control,* vol. 2, pp. 234-246, March 1996.

[17] R. C. Chan*, et al.*, "OCT-based arterial elastography: robust estimation exploiting tissue biomechanics," *Optics Express,* vol. 19, pp. 4558-4572, June 2004.

[18] G. van Soest*, et al.*, "Robust Intravascular Optical Coherence Elastography by Line Correlations," *Physics in Medicine and Biology,* pp. 2445-2458, 2007.

[19] G. J. Tearney*, et al.*, "Consensus Standards for Acquisition, Measurement, and Reporting of Intravascular Optical Coherence Tomography Studies A Report From the International Working Group for Intravascular Optical Coherence Tomography Standardization and Validation," *Journal of the American College of Cardiology,* vol. 59, pp. 1058-1072, 2012.

[20] J. E. Crouch and J. R. McClintic, *Human anatomy and physiology*. New York, London, Sydney, Toronto: John Wiley & Sons, Inc., 1971.

[21] Y. C. Fung, *Biomechanics; Motion, Flow, Stress, and Growth*. New York, Berlin, Heidelberg: Springer, 1990.
[22] U. Haberland*, et al.*, "Investigation of highly scattering media using near-infrared continuous wave tunable semiconductor laser," in *SPIE*, 1995.
[23] R. K. Wang*, et al.*, "Tissue Doppler optical coherence elastography for real time strain rate and strain mapping of soft tissue," *Applied Physics Letters,* vol. 89, pp. 144103-1 - 144103-3, 2006.
[24] R. K. Wang*, et al.*, "Phase-sensitive optical coherence elastography for mapping tissue microstrains in real time," *Applied Physics Letters,* vol. 90, pp. 164105-1 - 164105-3, 2007.
[25] R. Karimi*, et al.*, "A Novel Framework for Elastography and Modulus Estimation: Integration of Tissue Mechanics with Imaging," in *Proceedings of 3rd IEEE International Symposium on Biomedical Imaging: From Nano to Macro*, 2006, pp. 602-605.
[26] K. K. C. Lee*, et al.*, "Real-time speckle variance swept-source optical coherence tomography using a graphics processing unit," *Biomedical Optics Express,* vol. 3, p. 8, 2012.
[27] B. J. Vakoc*, et al.*, "Phase-resolved optical frequency domain imaging," *Optics Express,* vol. 13, p. 11, 2005.
[28] T. C. Chu*, et al.*, "Application of Digital-Image-Correlation Techniques to Experimental Mechanics," *Experimental Mechanics,* vol. 25, pp. 232 - 244, 1985.
[29] H. A. Bruck*, et al.*, "Digital Image Correlation Using Newton-Raphson Method of Partial Differential Correction," *Experimental Mechanics,* vol. 29, pp. 261 - 267, 1989.
[30] I. Dragan*, et al.*, "Bilinear interpolation from polar to rectangular point raster for inverse problem solving," in *Mathematical Methods in Electromagnetic Theory*, Lviv, 1996, pp. 429 - 431.
[31] K. H. Y. Cheng*, et al.*, "Endovascular optical coherence tomography intensity kurtosis: visualization of vasa vasorum in porcine carotid artery," *Biomedical Optics Express,* vol. 3, pp. 388 - 399, 2012.
[32] C. Kasai*, et al.*, "Real-Time Two-Dimensional Blood Flow Imaging Using an Autocorrelation Technique," *IEEE Transactions on Sonics and Ultrasonics,* vol. SU-32, p. 7, 1985.
[33] D. C. Ghiglia and M. D. Pritt, *Two-Dimensional Phase Unwrapping: Theory, Algorithms and Software*. New York: Wiley-Interscience, 1998.
[34] A. M. Malek*, et al.*, "Hemodynamic Shear Stress and Its Role in Atherosclerosis," *The Journal of the American Medical Association,* vol. 282, pp. 2035 - 2042, 1999.
[35] F. J. H. Gijsen*, et al.*, "Strain distribution over plaques in human coronary arteries relates to shear stress," *Am. J. Physiol - Heart and Circulatory Physiology,* vol. 295, pp. H1608 - H1614, 2008.
[36] D. L. Fry, "Acute Vascular Endothelial Changes Associated with Increased Blood Velocity Gradients," *Circulation Research,* vol. 22, pp. 165 - 197, 1968.
[37] M. D. Kulkarni*, et al.*, "Velocity-estimation accuracy and frame-rate limitations in color Doppler optical coherence tomography," *Optics Letters,* vol. 23, pp. 1057 - 1059, 1998.